Deliverable 5.4 - Final report on the evaluation of the tasks of the workpackage 2 - FLUid Image analysis and Description (FLUID) - Project No. FP6-513663 - FET Open - Domain, Priority IST

Dominique Heitz, Johan Carlier, Georges Arroyo

FLUid Image analysis and Description (FLUID)
Project No. FP6-513663
FET - Open Domain, Priority IST

Deliverable 5.4

Final report on the evaluation of the tasks of the workpackage 2

Dominique Heitz[1], Johan Carlier and Georges Arroyo

Cemagref

Due date of deliverable:	30 May 2007
Actual submission date:	30 May 2007
Start date of project:	1 December 2004
Duration:	3 years

Project cofunded by the European Comission
within the Sixth Framework Programme (2002-2006).

Dissemination level: PU (Public) Revision: 1

[1] dominique.heitz@cemagref.fr

Abstract

This document is the final report on the evaluation of the tasks of the workpackage 2. It gives results of the statistical evaluation of 2D/3D turbulent shear flows estimations with optical flow approaches, developped within workpackage 2 of the project FLUID. Three approaches are evaluated: OF1, a variational fluid dedicated optical flow estimator (Corpetti *et al.*, 2006); OF2, a variational motion estimator for incompressible flows (Yuan *et al.*, 2007); COROF1, a collaborative correlation - variational approach for robust optical flow estimation (Héas *et al.*, 2007; Heitz *et al.*, 2007).

Contents

Chapter 1

Introduction

In this chapter we describe the global objectives of the evaluation, the fluid mechanics database designed for the FLUID project, the global procedure of evaluation of WP2, WP3 and WP4, and the goal of the preliminary evaluation of the WP2 presented in this document.

1.1 Evaluation objectives

The aim of the evaluation is to present, discuss and analyze the results from the different algorithms on the image database. Detailed and quantitative comparisons will be undertaken in order to provide a feedback to improve the different methods. The comparison of the results obtained by the different approachs will be performed and presented at the next meetings and in the the deliverables D5.1 to D5.6. Statistical quantities and spectra will be looked at in order to evaluate the capability of the methods to analyse 2D and 3D turbulent flows. The database is composed of simple analytical flows, 2D and 3D turbulent flows, couple of images and time resolved image sequences, particle and scalar images.

1.2 Fluid mechanics database for the evaluation

A database of particle and scalar images was designed for analysis. All images in this database are suitable for variational approaches. Correlation analysis can also be done except maybe for scalar images. The database is organized in three packages. Details on the characteristics of flows and images are given in the documents, delivered by Johan Carlier (.FlUID-website ./WP01/package_02_readme_Cemagref.pdf).

The first group is composed of simple analytical solutions. Seven subcases have been provided:

Case n^o	Description	Provider	Image type	Seeding	Number of sets
A	**Viscous and potential flows**	Cemagref	synthetic	particle	
A1	Poiseuille	Cemagref	synthetic	particle	A1(41)
A2	Lamb-Oseen vortex	Cemagref	synthetic	particle	A2(41)
A3	Uniform flow	Cemagref	synthetic	particle	A3(41)
A4	Sink flow	Cemagref	synthetic	particle	A4(41)
A5	Vortex flow	Cemagref	synthetic	particle	A5(41)
A6	Cylinder with circulation	Cemagref	synthetic	particle	A6(41)
A7	PIV-Challenge 2005	LaVision	synthetic	particle	A7(2)

The second group is composed of two dimensional turbulent flows obtained by experimental and numerical approaches. Two subcases have been provided for the numerical approach:

Case n°	Description	Provider	Image type	Seeding	Number of sets
B	**Exp. of 2D turbulent flow**	LPS-ENS	real	fluorescein	B(96)
C	**DNS of 2D turbulent flow**[a]	Cemagref	synthetic		
C1a	Time resolved $\Delta T = 10\delta t$[b]	Cemagref	synthetic	particle	C1a(1000)
C1b	Time resolved $\Delta T = 10\delta t$	Cemagref	synthetic	temperature	C1b(1000)
C2	Time resolved $\Delta T = \delta t$	Cemagref	synthetic	particle	C2(200)

[a]Direct Numerical Simulation (DNS).
[b]ΔT is the time step beetwen two images and δt is the time step for the Direct Numerical Simulation

The third group is composed of three dimensional turbulent flows obtained by experimental and numerical approaches. Ten subcases have been provided:

Case n°	Description	Provider	Image type	Seeding	Number of sets
D	**Exp. of turbulent wake**	Cemagref	real	particle	
D1	Far wake ($x/D = 30$)	Cemagref	real	particle	D1(5000)
D2	Near wake ($x/D = 0$)	Cemagref	real	particle	D2(5000)
D3	*Near wake - Time resolved*	*Cemagref*	*real*	*particle*	*D3(xxx)*
E	**LES of turbulent wake**[a]	Cemagref	synthetic		
E1	Volume	Cemagref	synthetic	particle	E1(10)
E2	Time resolved	Cemagref	synthetic	particle	E2(200)
F	**Time-Resolved 2D2C PIV**	LaVision	real	particle	F(xx)
G	**3D synthetic data**	LaVision	synthetic	particle	
G1	constant velocity	LaVision	synthetic	particle	G1(xx)
G2	compression wave	LaVision	synthetic	particle	G2(xx)
G3	compression wave + gradient	LaVision	synthetic	particle	G3(xx)
G4	shear flow	LaVision	synthetic	particle	G4(xx)
G5	shear flow + gradient	LaVision	synthetic	particle	G5(xx)

[a]Large Eddy Simulation (LES) of the wake of a circular cylinder at $Re = 3900$.

According to the recommendations of the first review of the FLUID project, a new case (case D2) will be provided. This case will include a reference flow solution obtained using the result of an optimized experiment (zoom in the flow, high image quality). Then the data set containing images for the analysis will be acquired in more realistic situations (non-optimal conditions: limited spatial resolution, constrast etc.).

1.2.1 Database location

The data of the different cases have been provided either on the FLUID website or on portable hard-disks (USB-HDD) sent to each group involved in the project.

Case n^o	Description	Directory
A1a	Poiseuille	FLUID-website ./WP01/package_01_Cemagref/
A2a	Lamb-Oseen vortex	FLUID-website ./WP01/package_01_Cemagref/
A3a	Uniform flow	FLUID-website ./WP01/package_01_Cemagref/
A4a	Sink flow	FLUID-website ./WP01/package_01_Cemagref/
A5a	Vortex flow	FLUID-website ./WP01/package_01_Cemagref/
A6a	Cylinder with circulation	FLUID-website ./WP01/package_01_Cemagref/
A1b	Poiseuille	USB-HDD ./package_02/analytic/
A2b	Lamb-Oseen vortex	USB-HDD ./package_02/analytic/
A3b	Uniform flow	USB-HDD ./package_02/analytic/
A4b	Sink flow	USB-HDD ./package_02/analytic/
A5b	Vortex flow	USB-HDD ./package_02/analytic/
A6b	Cylinder with circulation	USB-HDD ./package_02/analytic/
A7	single synthetic PIV image	FLUID-website ./WP01/package_04_LaVision/
B	Exp. of 2D turbulent flow	USB-HDD ./package_02/exp_turb2d/
C1a	DNS Turb 2D Time resolved	USB-HDD ./package_02/dns_turb2d/run02/particle/
C1b	DNS Turb 2D Time resolved	USB-HDD ./package_02/dns_turb2d/run02/scalar/
C2	DNS Turb 2D Time resolved	USB-HDD ./package_02/dns_turb2d/run12/
D1	Exp. far wake	USB-HDD ./package_02/exp_wake/
D2	*Exp. near wake*	
D3	*Exp. near wake - Time resolved*	
E1	LES wake - Volume	USB-HDD ./package_02/les_wake/
E2	*LES wake - Time resolved*	
F	real high-speed PIV images	FLUID-website ./WP01/package_03_LaVision/
G1	Volume - constant velocity	FLUID-website ./WP01/package_06_LaVision/
G2	Volume - compression wave	FLUID-website ./WP01/package_06_LaVision/
G3	Volume - comp. wave + gradient	FLUID-website ./WP01/package_06_LaVision/
G4	Volume - shear flow	FLUID-website ./WP01/package_06_LaVision/
G5	Volume - shear flow + gradient	FLUID-website ./WP01/package_06_LaVision/

1.3 Evaluation procedure

1.3.1 Generalities

Tasks of workpackages 2, 3 and 4 will be evaluated with the database presented above. The first group can be used by developpers to provide simple validations of their methods. These images include divergence and rotational free flows (potential flows), which can show immediately the capability of the algorithms to estimate correctly these quantities. The case A7 provided by LaVision, including differents degrees of local flow gradients without and with varying degrees of image noise, can show immediately in a visual as quantitative way the strengths and weaknesses of the algorithms.

According to the recommendations of the first FLUID project review, mainly groups 2 and 3 will be considered for the evaluation procedure. Indeed, the validation will be focused on the cases considering turbulent flows, obtained with experiments or numerical simulations. The case G including 3D-synthetic data will also be considered since it contributes to innovative aspects in the project (evaluation of 3D3C methods).

Depending on the different cases the ground truth will be provided by analytical expressions, DNS/LES solutions, controlled PIV measurements or hot-wire anemometry measurements.

1.3.2 Format of results

The results of the analysis have to be provided by contributors in ASCII format compatible with gnuplot and tecplot : $(x, y, u, v, w, \text{flag})$ with a tab character to separate each column and a blank line (carriage return) to separate each block of y fixed coordinates. The results have to be given in pixel units with the origin on the bottom left border of the image. x, y and flag (optional) have to be in integer format. u, v and w have to be in float format (simple precision). If your method provides vectors with subpixel location, x and y can be given in float format (simple precision). The optional flag can be provided if you want to give information on each individual vector. The flag definition should be provided in a separate file. An example of file structure is presented below.

```
# If you want to add a comment.
 x1  y1  u  v  w  f
 x2  y1  u  v  w  f
 .
 .
 .
 xn  y1  u  v  w  f

 x1  y2  u  v  w  f
 x2  y2  u  v  w  f
 .
 .
 .
 xn  y2  u  v  w  f

...

 x1  ym  u  v  w  f
 x2  ym  u  v  w  f
 .
 .
 .
 xn  ym  u  v  w  f
```

An acronym and a number must appear in the name of all the files you will provide. For instance a00001_cvgpr_01.txt contains the vector map of the computation 01 obtained by CVGPR-group from the set of images a00001a.tif and a00001b.tif. If you have different methods or if you use different parameters, use the number after the acronym to distinguish them. Define this number in a separate file.

1.3.3 Evaluation of 2D2C methods

Compute cases A7, B, C1, C2, C3, D1, *E2* and F.

1.3.4 Evaluation of time resolved methods

Compute cases C1, C2, C3, *E2* and F.

1.3.5 Evaluation of 3D3C methods

Compute cases E1, G1, G2, G3, G4, G5.

Acronym	Approach	Group	Reference	Description
OF1	optical-flow	INRIA	Corpetti *et al.* (2002*a*, 2006)	§3.1
OF2	optical-flow	CVGPR	Yuan *et al.* (2005, 2007)	§3.2
COROF1	correlation/optical-flow	INRIA	Héas *et al.* (2007); Heitz *et al.* (2007)	§3.3

Table 1.1: Approaches developped in WP2 and evaluated in the present document.

1.3.6 Computation of cases C3 and D1

Case C3: Compute image 0 and image 9, image 0 and image 19, ... up to image 0 and image 199, with the same set of parameters for the 19 couples of images. Compute the same set of images as many time you change the set of parameters (see §1.3.2 for the name of the files).

Case D1: In order to reduce the computational time and the size of the results you can crop the images before computation. With the origin of the image coordinate system on the bottom left, crop the image from $(275, 0)$ (bottom-left) to $(787, 1024)$ (top-right).

1.4 Evaluation of workpackage 2

This section describes briefly the approaches to evaluate and the database considered for this preliminary evluation.

1.4.1 Approaches evaluated

Three approaches developped in WP2 were evaluated (cf. Tab 1.1): OF1, an optical-flow technique developped by INRIA group; OF2, an optical-flow technique developped by CVGPR group; and COROF1, a collaborative correlation/optical-flow technique developped by INRIA group in collaboration with Cemagref group.

Depending on the database considered the obtained results were compared with the information provided by correlation techniques[1], hot-wire anemometry and direct numerical simulations.

1.4.2 Database considered

OF1 approach was evaluated in three steps. First we used a set of data available from the very beginning of the FLUID project (experiments in a plane turbulent mixing layer and in the near wake of a circular cylinder, synthetic image of the visualization society of japan (VSJ)). Then, we participated to the PIVChallenge 2005. And finally, the database of the FLUID project was used (cases C1a, C1b and D1).

OF2 approach was evaluated with the database of the FLUID project (cases C1a, C1b and D1).

COROF1 approach was evaluated with the database of the FLUID project (cases C2, D1 and F). In a preliminary evaluation, the database of the PIVChallenge 2005 (case B from C. Kaehler) was used (Heitz *et al.*, 2006).

[1]The results obtained with correlation approach were provided either by Bernd Wieneke with LaVision software (Davis), or by the Cemagref with LaVision software.

Chapter 2

Database description

This chapter describes the database used to perform the evaluation of the workpackage 2. §2.1, §2.2 and §2.3 present a set of data available from the very beginning of the FLUID project and used to evaluate OF1 approach. §2.4 present three cases of the PIV Challenge 2005 used to evaluate OF1 and COROF1 approaches. Finally, §2.5 and §2.6 describe cases C1a, C1b, C2 and D1, designed for the FLUID project, and used to evaluate OF1, OF2 and COROF1 approaches.

2.1 Experiments in a turbulent plane mixing layer

The mixing layer studied here was generated in a closed circuit, subsonic wind tunnel R300 of the CEAT (Centre d'Études Aérodynamiques et Thermiques, University of Poitiers, France). This wind tunnel has a square test section of cross-sectional dimensions 300 mm $\times$ 300 mm and length 2 m, with a contraction ratio of 10. The one stream blow generated by a fan is divided by a splitter plate in two separated streams flowing through two different head loss devices, followed by fine mesh screens, and are jointly released at the end of the splitter plate to give a two-stream flow with low initial turbulence level. Tripping wire were used on both sides of the splitter plate to ensure a rapid and uniform transition of the boundary layer well upstream of the trailing edge. Hence, the mixing layer was initially turbulent. Wind-tunnel ceiling was tilted to achieve a negligible streamwise pressure gradient. For more details about the facility, the reader can refer to Heitz (1999). The velocity ratio of the two streams $r = U_\mathrm{a}/U_\mathrm{b}$ ($U_\mathrm{a} = 9$ m s^{-1} and $U_\mathrm{b} = 6$ m s^{-1}) was 0.67 with an average advective velocity $U_\mathrm{m} = (U_a + U_b)/2$ of 7.5 m s^{-1}. The turbulence intensity corresponding to free stream velocity is less than 0.3%. The location of the origin of the x axis corresponds to the position where the vorticity thickness of the mixing layer δ_ω equaled 15 mm and was found 240 mm downstream of the trailing edge of the splitter plate. In all the figures presented in chapter 4 this value was employed to reduce x and y coordinates.

2.2 Experiments in the wake of a circular cylinder at Re=3000

The experiments in the near wake of a circular cylinder were carried out in a small opened wind tunnel of the Cemagref (Center of Rennes – France), having a test section 142 mm wide 142 mm high, and 1100 mm long. The wind tunnel consists of a blower supplying air to a conditioning system composed of a honeycomb and a porous media (foam) followed by a 2:1 contraction, which provided a free-stream uniformity and a turbulence intensity less than 0.1%. The flow velocity was 4.5 m s^{-1}. The circular cylinder had a cross-sectional diameter $D = 10$ mm and a length $L = 142$ mm, giving an aspect ratio of $L/D = 14.2$. The value of the Reynolds number based on the diameter D was $Re = 3000$. The cylinder was mounted vertically and no end plates were used to limitate end effects.

2.3 VSJ standard image-pairs

The Visualization Society of Japan (VSJ) developed in 1999 PIV standard images and PIV guide tools in order to popularize the PIV techniques. Within this project, many synthetic PIV image sequences, called "Standard Images", were generated along with the corresponding ground truth velocity vector fields in a wide variety of controlled conditions (Okamoto *et al.*, 2000). They are available on the internet. The parameters of the eight standard situations tested in this paper are listed in table 2.1 and represent : the number N of particles that are present in the images, the particle diameter D_m associated to its standard deviation D_s, the average image velocity v_m and the out-of-plane velocity w_m. Compared to image pair #1, the pairs #2 and #3 differ only with respect to the magnitude of the flow field; the image pairs #4 and #5 have only different number of particle; the pairs #6 and #7 have particles with a different diameter while the pair #8 has a high out of plane velocity.

Some results on these images are available in the literature (Quénot, 1999; Ruhnau *et al.*, 2005). We used the relative L_1 norm error (L_1 norm of the difference between the correct and computed velocities in pixels/frame divided by the average in-plane velocity) to compare the different motion fields.

	N	T	$\boldsymbol{v}_m$	w_m	D_m	D_s
#1	4000	33	7.39	0.017	5.0	1.4
#2	4000	100	22.4	0.058	5.0	1.4
#3	4000	10	2.24	0.006	5.0	1.4
#4	10000	33	7.39	0.017	5.0	1.4
#5	1000	33	7.39	0.017	5.0	1.4
#6	4000	33	7.39	0.017	5.0	0.0
#7	4000	33	7.39	0.017	10.0	4.0
#8	4000	33	7.39	0.170	5.0	1.4

Table 2.1: Main characteristics of the 8 standard VSJ image-pairs.

2.4 PIV Challenge 2005

The Cemagref, in collaboration with INRIA, have submitted a dense optical flow method dedicated to fluid flows to the PIV challenge 2005. This challenge which aims at comparing different motion estimator for images of fluid flows seeded with particle held in Pasadena, California in September 2005 (http://www.pivchallenge.org/). Three cases were used for this preliminary evaluation: case A2 from M. Stanislas based on a synthetic turbulence with a spectrum slope equal to -3; case A3 from M. Stanislas based on the direct numerical simulation of a stratified flow; case B from C. Kaehler based on a DNS and simulating a time resolved PIV in a channel.

2.5 DNS of 2D turbulence

The main interest of a synthetic image sequence database of numerically generated $2D$ turbulent flow fields is the knowledge of the exact solution along the time for flow with a large scale range in the energy spectrum. For this purpose, DNS was perfomed to solve particle and scalar transport in $2D$ sustained turbulent flow by the Cemagref. The general description of the code can be found a document available on the FLUID project web-site (./WP01/package_02_readme_Cemagref.pdf).

The vorticity and scalar equations are solved in Fourier space using dealiased Fourier expansions in two directions with periodic boundary conditions. The time integration is third-order/three steps with a Runge-Kutta scheme. The code is called pseudo-spectral.

The coordinates of the particules are solved in the physical space inside the vorticity equation computation using the same Runge-Kutta scheme in order to use the intermediate velocity components u and v. However, an interpolation (bicubic) of the velocity field has to be applied as the particles are not supposed to be located on the nodes of the grid.

For the FLUID project, sustaining turbulence along the time is of great interest to allow time averaging of statistical quantities in the post-processing, for evaluation purposes. Then, the vorticity equation was slighty modified with a forcing term proportional to the vorticity and random on the Fourier coefficients, and a friction term added only for the first modes. That resulted in enstrophy injection dissipated by small scale and the energy injection dissipated by large scales (see figure 2.1).

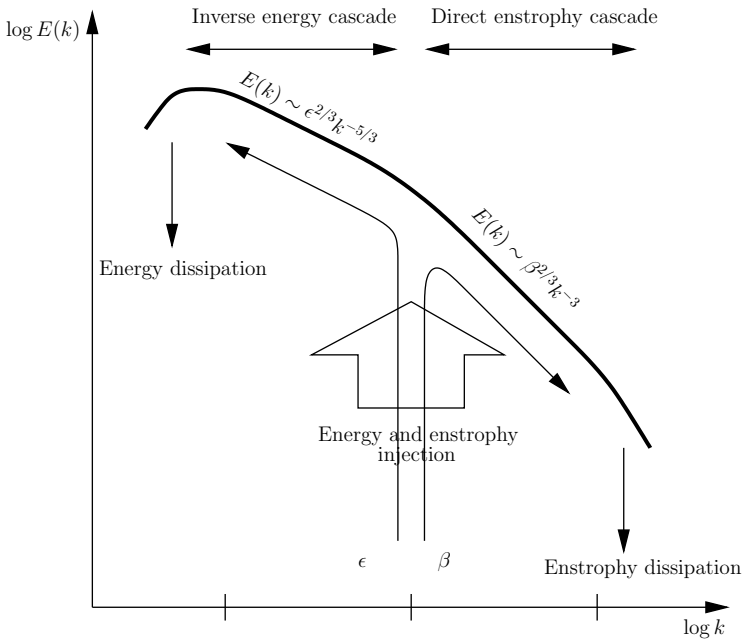

Figure 2.1: Energy and enstrophy cascade

2.5.1 Set of images delivered

Different sets of parameters have been tested. The strategy was to select the maximum number of nodes for a reasonable computation time with the computer available, the maximum Re and Pe for this grid size and a target Energy/Enstrophy injection which could be dissipated by the system. Finally, two sets of parameters were selected as summarized below in table 2.2. In run 12, used to generate case C2, only particles were transported. In run 02, used to generate cases C1a and C1b, both particles and scalar were transported. Case C2 consists of a sequence of 200 successive images ($1\,024 \times 1\,024$ px^2) with a time separation $\Delta t = 0.001$. Cases C1a and C1b consist of sequences of 1 000 successive images (256×256 px^2) with a time separation $10\Delta t = 0.1$. Fig. 2.2 presents two samples of the scalar images and the corresponding particle images at different times.

2.6 Experiments in the wake of circular cylinder at Re=3900

This section describes a $2D$-$2C$ PIV experiment carried out in one of the wind tunnels of the Cemagref (Rennes Regional Centre).

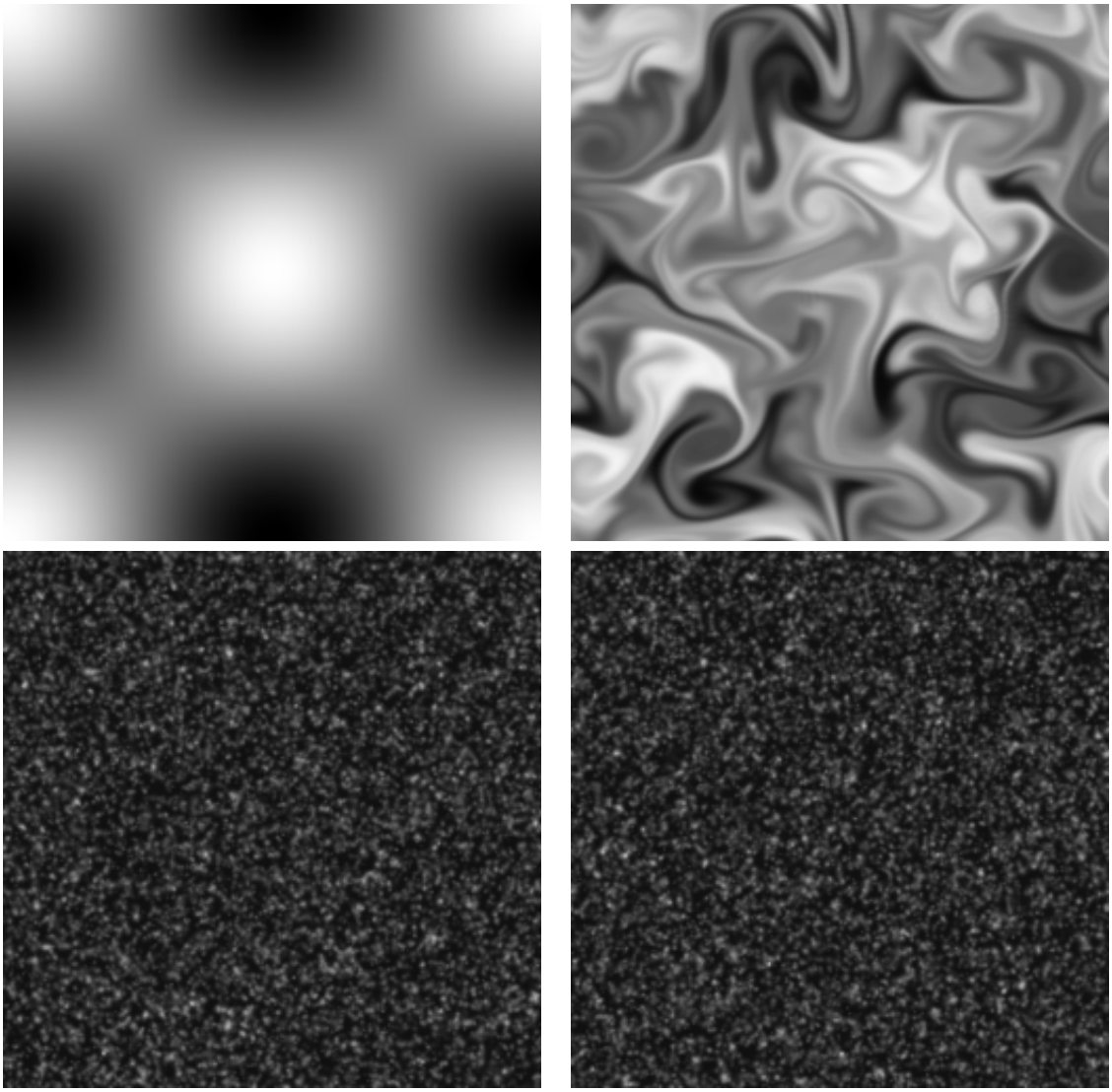

Figure 2.2: Two samples of the scalar images and the corresponding particle images.

Corresponding case	C2	C1a C1b
Run	12	02
Number of nodes	$1\,024 \times 1\,024$	256×256
cfl	0.5	0.5
Re	30 000	3 000
Re_ν	5	5
Pe	no scalar	2 100
Sc	no scalar	0.7
Location of the initial maximum	40	40
Forcing band	$[5; 10]$	$[5; 10]$
Target enstrophy dissipation	0.1	0.1
Proportion of random/proportional forcing	0.5	0.5
Time step Δt	0.001	0.01
Size box	2π	2π

Table 2.2: DNS used to generate case C1a, C1b and C2.

Case n^o	Description	Directory
C1a	DNS Turb 2D Time resolved	USB-HDD ./package_02/dns_turb2d/run02/particle/
C1b	DNS Turb 2D Time resolved	USB-HDD ./package_02/dns_turb2d/run02/scalar/
C2	DNS Turb 2D Time resolved	USB-HDD ./package_02/dns_turb2d/run12/

Table 2.3: Cases considered in the present evaluation.

2.6.1 Wind tunnel

The sketch (in front view) of the wind tunnel used in this experiment is presented in Fig. 2.3. The aeraulic circuit is mainly made of a centrifugal fan, a diffuser, a plenum chamber with honey comb and grids, a convergent with a contraction coefficient of 4 and a testing zone with transparent walls. The testing zone is squared in cross section with 280 mm of with dimensions and 100 cm in length. The upper wall is slightly tilted to suppress the longitudinal pressure gradient. The flow velocity can be chosen continuously between 1 and 8 m. s^{-1} with a good stability. The uniformity of the velocity profile at the entrance of test section was checked by hot-wire anemometry. The free stream turbulence intensity was less than 0.5%. The temperature was kept within $\pm 0.2°$ C by using an air-water heat-exchanger.

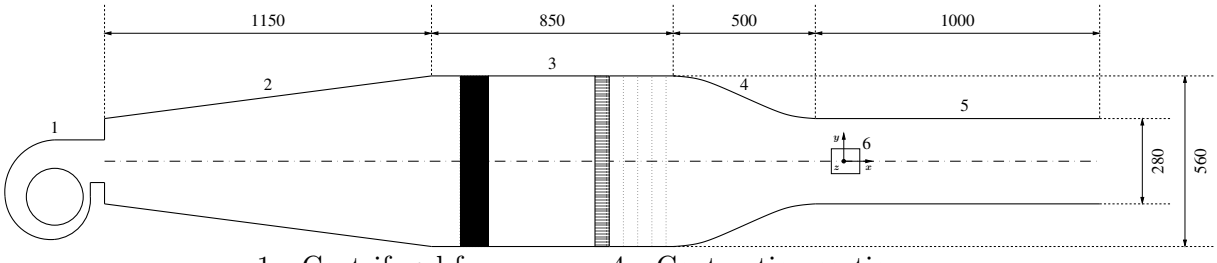

1 : Centrifugal fan
2 : Low divergent section
3 : Plenum chamber
4 : Contraction section
5 : Testing section
6 : Cylinder and end-plates

Figure 2.3: Front view of the windtunnel.

The circular cylinder had a length $L = 280$ mm and a diameter $D = 12$ mm. It was equipped

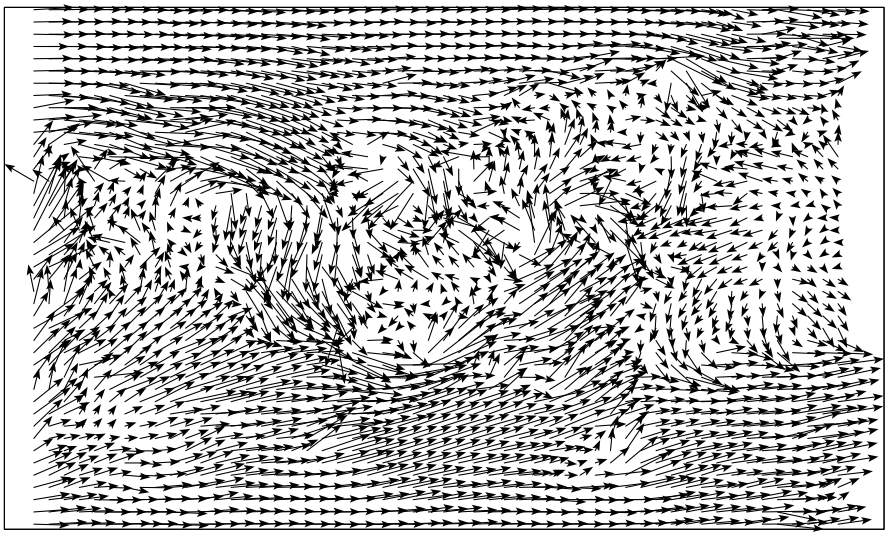

Figure 2.4: Structure of the velocity fields (a constant velocity component u was subtracted).

with 2 thin rectangular end plates. The distance between the end-plates was 240 mm providing an aspect ratio $L/D = 20$. The clearence between the walls and the end-plates was about 20 mm which was much larger than the thickness of the boundary layer on the wall. The blockage ratio was 4.3%. The circular cylinder was mounted horizontaly at $3.5D$ from the entrance of the testing zone.

The reference frame is direct and the origin is located at the center of the cylinder. The longitudinal x-axis is the testing zone axis of the wind tunnel, y-axis is normal to the wake central plane (symmetry plane) and z-axis is the cylinder axis. u, v and w are the velocity components related to x, y and z axis respectively.

2.6.2 Measurements

$2D$-$2C$ PIV experiments (2 in-plane velocity components in a plane field) were carried out with NewWave Solo 3 Nd-YAG laser (Energy by pulse of 50 mJ) and a SensiCam PCO cameras (CCD size of 1280×1024 px^2 and dynamics of 12 bits). The laser sheet was produced by means of a Rodenstock telescope and a cylindrical lens. The diameter of the particle seeding (diluted polyglycol in water) was less than 10 μm. The measurement area was located in the near wake and at $30D$ behind the circular cylinder, in the plane $z = 0$. The camera was located perpendicularly to the laser sheet at a distance of 100 cm. For the mounted lens, the focal length was 105 mm with an aperture of 5.6. The resulting field of view was about $8D \times 6.4D$. The free-stream velocity was adjusted at 4.8 m. s^{-1} so that the Reynolds number Re_D be 3 900 (Reynolds number based on the free stream velocity Ue, the cinematic viscosity ν and the diameter of the circular cylinder D). 5 000 image pairs were obtained with a time interval of 200 μs. To give an idea of the flow structure, Fig. 2.4 shows a modified velocity field where a constant velocity component was substracted (calculated with a classical PIV algorithm).

2.6.3 Set of images delivered

5 000 image pairs were delivered in TIF-format with 16 bits in depth[1] (see Tab. 2.4). The exact image size is 96.38 mm in length (1 280 px) and 77.03 mm in height (1 024 px).

Case n°	Description	Directory
D1	Exp. far wake	USB-HDD ./package_02/exp_wake/
D2	Exp. near wake	

Table 2.4: Case considered in the present evaluation

2.7 Slightly turbulent air flow

The images show a slightly turbulent air flow with small water droplets with a diameter of about 5 μ m. The sequence has been recorded with a Photron APX camera with 1024 $\times$ 1024 px running at 1 khz. The field of view is about $7 \times 7 \text{cm}^2$. The sequence has been selected to show typical problems in PIV recordings. The seeding density is quite inhomogeneous even with regions without any seeding particles.

Figure 2.5: Time-resolved images of a slightly turbulent air flow

Case n°	Description	Directory
F	real high-speed PIV images	FLUID-website ./WP01/package$_0$3$_L aVision$/

Table 2.5: Case considered in the present evaluation

[1]With classical viewer, the images may appear relatively black and seem to be poorly enlighted. In fact, the original images are 12 bits in depth and are converted for more convenience in TIF-format with 16 bits in depth, giving artificially low values as compared to the global 16 bits range.

Chapter 3

Description of the methods

This chapter describes the differente approaches evaluated. §3.1 presents a dense estimator with fluid dedicated optical flow, named OF1 in the present document. §3.2 presents a variational motion estimation for incompressible flows, named OF2 in the present document. §3.3 presents a collaborative scheme for robust optical flow estimation, named COROF1 in the present document.

3.1 Dense estimation with fluid dedicated optical flow

The optical flow scheme presented below and evaluated in 4.1 was proposed by INRIA. This section is a part of Corpetti *et al.* (2006).

Obtaining the *optical-flow* consists in estimating a dense motion field from two consecutive images. As previously mentioned, many methods have been proposed the last two decades to estimate such an optical-flow. Most of them are based on the seminal work of Horn & Schunck (1981*a*). In this section, optical-flow methods will then refer to this latter definition. It is nevertheless important to point out that some authors propose reliable optical-flow computations not based on Horn & Schunck (1981*a*), especially for PIV images in Quenot *et al.* (1998) where the authors use dynamic programming and orthogonal algorithms. The reader will find in Barron *et al.* (1994) a survey of different methods for computing optical flow (differential techniques, region based matching, energy based methods and phase based techniques).

3.1.1 Generic optical-flow estimator

The most accurate techniques to address the generic problem of estimating the apparent motion from image sequences are based on the seminal work by Horn & Schunck (1981*a*). These techniques are based on the minimization of a global cost function $\mathcal{H}$ composed of two terms. The first one, named "observation term", is derived from a *brightness constancy* assumption and assumes that a given point keeps the same intensity along its trajectory. It is expressed through the well known *optical flow constraint equation* (OFCE):

$$\mathcal{H}_{obs}(E,\boldsymbol{v}) = \iint_{\Omega} \Psi_1\left[\nabla E(\boldsymbol{x},t)\cdot\boldsymbol{v}(\boldsymbol{x},t) + \frac{\partial E(\boldsymbol{x},t)}{\partial t}\right]d\boldsymbol{x}, \tag{3.1}$$

where $\boldsymbol{v}(\boldsymbol{x},t) = (u,v)^T$ is the unknown velocity field at time t and location $\boldsymbol{x} = (x,y)$ in the image plane Ω, $E(\boldsymbol{x},t)$ is the image brightness, viewed for a while as a continuous function. This first term relies on the assumption that the visible points conserve roughly their intensity in the course of a small displacement.

$$\frac{dE}{dt} = \nabla E\cdot\boldsymbol{v} + \frac{\partial E}{\partial t} \approx 0. \tag{3.2}$$

The associated penalty function Ψ_1 is often the L_2 norm. However, better estimates are usually obtained by choosing a "softer" penalty function (Black, 1994; Mémin & Pérez, 1998*a*). Such functions, arising from robust statistics (Huber, 1981), limit the impact of the many locations where the brightness constancy assumption does not hold, such as on occlusion boundaries. Appendix A.2 briefly presents the robust estimators used.

This single (scalar) observation term does not allow to estimate the two components u and v of the velocity. In order to solve this ill-posed problem, it is common to employ an additional smoothness constraint $\mathcal{H}_{reg}$. Usually, this second term enforces a spatial smoothness coherence of the flow field. It relies on a contextual assumption which enforces a spatial smoothness of the solution. This term usually reads:

$$\mathcal{H}_{reg}(\boldsymbol{v}) = \iint_{\Omega} \Psi_2\big[|\nabla u(\boldsymbol{x},t)| + |\nabla v(\boldsymbol{x},t)|\big], \tag{3.3}$$

As with the penalty function in the data term, the penalty function Ψ_2 was taken as a quadratic in early studies, but a softer penalty is now preferred in order not to smooth out the natural discontinuities (boundaries, ...) of the velocity field (Black, 1994; Cohen & Herlin, 1999; Kornprobst *et al.*, 1999; Mémin & Pérez, 1998*a*). Based on (3.1) and (3.3), the estimation of motion can be done by minimizing:

$$\begin{aligned}\mathcal{H}(E,\boldsymbol{v}) &= \mathcal{H}_{obs}(E,\boldsymbol{v}) + \alpha\mathcal{H}_{reg}(\boldsymbol{v}) \\ &= \iint_{\Omega} \Psi_1\left[\nabla E(\boldsymbol{x},t)\cdot\boldsymbol{v}(\boldsymbol{x},t) + \frac{\partial E(\boldsymbol{x},t)}{\partial t}\right]d\boldsymbol{x} + \\ &\alpha\iint_{\Omega} \Psi_2\big[|\nabla u(\boldsymbol{x},t)| + |\nabla v(\boldsymbol{x},t)|\big],\end{aligned} \tag{3.4}$$

where $\alpha > 0$ is a parameter controlling the balance between the smoothness constraint and the global adequacy to the observation assumption.

Due to its differential nature, the relation in (3.1) is only defined for infinitesimal displacements. To handle large displacements it is common to use the expression (3.1) of the brightness conservation in an integrated way:

$$E(\boldsymbol{x}+\boldsymbol{d}(\boldsymbol{x}), t+\Delta t) - E(\boldsymbol{x},t) \approx 0, \tag{3.5}$$

where Δt is the temporal sampling rate and $\boldsymbol{d}(\boldsymbol{x})$ is the *displacement* from time t to $t+\Delta t$ of the point located at position $\boldsymbol{x}$ at time t. This new form, valid whatever the magnitude of $\boldsymbol{d}(\boldsymbol{x})$ be, is however highly nonlinear in the unknown vector. As a consequence, almost all studies resort to a succession of linearizations around a previous estimate $\tilde{\boldsymbol{d}}(\boldsymbol{d})$ ($\boldsymbol{d}(\boldsymbol{x}) = \tilde{\boldsymbol{d}}(\boldsymbol{d}) + \boldsymbol{h}(\boldsymbol{x})$) embedded within a multiresolution scheme (using a bilinar interpolation for the projection). The new cost-function to be minimized with respect to the displacement increment $\boldsymbol{h}$ reads then:

$$\begin{aligned}\mathcal{H}(E,\boldsymbol{h}) = \iint_{\Omega} \Psi_1\Big[&\nabla E(\boldsymbol{x}+\tilde{\boldsymbol{d}}(\boldsymbol{x}), t+\Delta t)\cdot\boldsymbol{h}(\boldsymbol{x}) + E(\boldsymbol{x}+\tilde{\boldsymbol{d}}(\boldsymbol{x}), t+\Delta t) \\ &- E(\boldsymbol{x},t)\Big] + \alpha\Psi_2\big[|\nabla(\tilde{\boldsymbol{d}}+\boldsymbol{h})(\boldsymbol{x})|\big].\end{aligned} \tag{3.6}$$

The associated successive minizations are usually performed using efficient iterative methods (Mémin & Pérez, 1998*a*; Mémin & Pérez., 2002).

It is important to outline that such an estimator defined as the minimizer of $\mathcal{H}$ is generic. It is only based on the assumption of luminance conservation and of first-order spatial smoothness of the motion. Even if this kind of estimator has been successfully used for fluid motion (Bannehr

et al., 1996; Cohen & Herlin, 1999; Larsen *et al.*, 1998; Mémin & Pérez, 1999; Ruhnau *et al.*, 2005; Wallace & Foss, 1995), the underlying assumptions are far from being sound hypothesis for such an applicative domain. As a matter of fact, image sequences representing fluid phenomena exhibit areas where the luminance function undergoes high temporal variations along the motion. These areas are often the centre of tridimensional motions that cause the appearance or the disappearance of fluid matter within the bidimensional visualization plane. These regions are in addition associated to divergent motions which

influence greatly the shape of the velocity field in large surrounding areas. An accurate estimation of the 2D apparent motion in such regions is therefore of the highest importance and is hardly possible with the optical-flow constraint.

3.1.2 Fluid dedicated optical-flow estimator

In a recent paper Corpetti *et al.* (2002*b*) proposed an optical-flow technique specifically dedicated to image sequences depicting fluid flow phenomenona. This specialized optical-flow estimator relies on an adaptation of the functional data-model and smoothness term.

3.1.3 Continuity equation and data model

Instead of sticking to the intensity conservation assumption, the data-model that has been considered relies on the continuity equation:

$$\frac{\partial \chi}{\partial t} + \mathrm{div}(\chi \boldsymbol{v}) = 0, \tag{3.7}$$

where χ denotes the density of the fluid, $\boldsymbol{v}$ its 3D velocity and $\mathrm{div}\boldsymbol{v} = \frac{\partial u}{\partial x} + \frac{\partial v}{\partial y} + \frac{\partial w}{\partial z}$ stands for the divergence of the vector field $\boldsymbol{v} = (u, v, w)$. Simple manipulations yield the alternative writing:

$$\frac{d\chi}{dt} + \chi \mathrm{div}\boldsymbol{v} = 0. \tag{3.8}$$

When the divergence of the 3D apparent flow vanishes, this equation is of the same form as the 2D optical flow constraint on luminance. The continuity equation, originally introduced in Schunk (1984) as a data model for motion estimation of intensity time varying images, has been since incorporated in several works. It has been considered in the context of fluid imagery either for satellite meteorological images (Béréziat *et al.*, 2000; Corpetti *et al.*, 2002*b*; Zhou *et al.*, 2000) or for experimental fluid mechanics (Wildes *et al.*, 1997). It has also been introduced in medical imaging domain to recover 3D deformation fields of the heart (Song & Leahy, 1991) or to analyze blood flow (Amini, 1994). In all these cases, this model has been proved to represent an alternative to standard luminance constancy assumption.

The use of continuity equation for image sequences analysis relies on two hypotheses. First, the luminance function is assumed to be directly related to a passive quantity transported by the fluid. Secondly, the continuity equation which holds in 3D, is assumed to hold as well for the bidimensional motion field captured by the image sequence. This latter assumption has been theoretically established in the case of transmittance imaging by Fitzpatrick (1988) and extended by Wildes *et al.* (1997). The first assumption is difficult to validate, especially in meteorological images due to the complexity and the heterogeneity of the underlying physical processes. Nevertheless, as shown by several works, the use of the continuity equation in the case of meteorological data is appealing (Béréziat *et al.*, 2000; Zhou *et al.*, 2000). As the brightness consistency is obviously not verified in that type of images, the continuity equation provides an interesting alternative data-model. Instead of expressing a point-wise conservation of the luminance along the motion, this alternative model assumes the conservation of the total luminance of any moving element of the image. This constraint reads:

$$\frac{dE}{dt} + E\mathrm{div}\boldsymbol{v} = 0. \tag{3.9}$$

However, as OFC-based data models, a data-model based on the continuity equation is highly sensitive to the presence of noise and is very likely not to hold everywhere. Also, due to its differential nature, the continuity equation is not valid in case of large displacements. In fact, this equation concerns the *velocity* $\boldsymbol{v}$ and not *displacement* (Nomura *et al.*, 1991). Unlike the brightness constancy expressed as $E(\boldsymbol{s}+\boldsymbol{d}(\boldsymbol{s}),t+\Delta t)-E(\boldsymbol{s},t)=0$, which is explicitly based on displacement, the continuity equation (3.9), as it stands, cannot serve as the basis of an incremental data-model embedded in hierarchical estimation schemes. To cope with this problem, let us assume that the velocities are constant between the instants t and $t+\Delta t$. In that case, equation (3.9) constitutes a simple first-order differential equation which can be integrated from time t to time $t+\Delta t$ along trajectories. Setting $\Delta t=1$ for notational convenience, and incorporating the integral constraint thus obtained in a robust penalty function yields a new data-term:

$$\mathcal{H}_{obs}(\boldsymbol{d})=\iint_{\Omega}\Psi_1\left(E\left(\boldsymbol{s}+\boldsymbol{d}(\boldsymbol{s}),t+1\right)\exp\left(\mathrm{div}\boldsymbol{d}(\boldsymbol{s})\right)-E(\boldsymbol{s},t)\right)d\boldsymbol{s}, \tag{3.10}$$

where $\boldsymbol{d}(\boldsymbol{s})$ is now the displacement from time t to $t+\Delta t$ of a point located at position $\boldsymbol{x}$ at time t. This form is non-linear with respect to the unknown velocity field $\boldsymbol{d}$ to estimate. As mentioned in section 3.1.1, we then linearize equation (3.10) around a crude solution $\tilde{\boldsymbol{d}}$ and embed it in a multiresolution scheme. The new linearized observation term based on the Integrated Continuity Equation (ICE) is:

$$\begin{aligned}\mathcal{H}_{obs}(\boldsymbol{h})=\iint_{\Omega}\Psi_1\Big[\exp(\mathrm{div}\tilde{\boldsymbol{d}}(\boldsymbol{s}))\Big((\tilde{E}(\boldsymbol{s})\nabla\mathrm{div}\tilde{\boldsymbol{d}}(\boldsymbol{s})+\nabla\tilde{E}(\boldsymbol{s}))\cdot\boldsymbol{h}(\boldsymbol{s})\\ +\tilde{E}(\boldsymbol{s})\Big)-E(\boldsymbol{s})\Big]d\boldsymbol{s},\end{aligned} \tag{3.11}$$

where $\boldsymbol{h}=\boldsymbol{d}-\tilde{\boldsymbol{d}}$, and we introduce the compact notation $\tilde{E}(\boldsymbol{s})=E(\boldsymbol{s}+\tilde{\boldsymbol{d}}(\boldsymbol{s}),t+\Delta t)$. We now turn to the definition of the smoothness prior to be used in conjunction with this new data energy term.

3.1.4 Second order Div-Curl regularization

By using Euler-Lagrange conditions of optimality, it is readily demonstrated (see appendix A.1) that the standard first-order regularization functional :

$$\mathcal{H}_{reg}(\boldsymbol{v})=\iint_{\Omega}|\boldsymbol{\nabla}u(\boldsymbol{s})|^2+|\boldsymbol{\nabla}v(\boldsymbol{s})|^2d\boldsymbol{s}$$

is equivalent from the minimization point of view, to the so-called *div-curl* regularization functional (Suter, 1994*a*):

$$\mathcal{H}_{reg}(\boldsymbol{v})=\iint_{\Omega}\left(\mathrm{div}^2\boldsymbol{v}(\boldsymbol{s})+\mathrm{curl}^2\boldsymbol{v}(\boldsymbol{s})\right)d\boldsymbol{s}, \tag{3.12}$$

where $\mathrm{div}\boldsymbol{v}=\frac{\partial u}{\partial x}+\frac{\partial v}{\partial y}$ and $\mathrm{curl}\boldsymbol{v}=\frac{\partial v}{\partial x}-\frac{\partial u}{\partial y}$ are respectively the divergence and the vorticity of the motion field $\boldsymbol{v}=(u,v)$.

A first-order regularization therefore penalizes the amplitude of both the divergence and the vorticity of the vector field. For fluid motion estimation, this does not seem appropriate since the apparent velocity field normally exhibits compact areas with high values of vorticity and/or divergence. In addition, an under-estimation of the divergence would be all the more problematic in our case, because the data model includes an explicit use of this quantity. For

these reasons, it seems more appropriate to rely on a second-order div-curl regularization (Gupta & Prince, 1996; Suter, 1994*a*):

$$\mathcal{H}_{reg}(\boldsymbol{d}) = \iint_{\Omega} \Big(|\boldsymbol{\nabla} \mathrm{div}\boldsymbol{d}(\boldsymbol{x})|^2 + |\boldsymbol{\nabla} \mathrm{curl}\boldsymbol{d}(\boldsymbol{x})|^2 \Big) d\boldsymbol{s}. \tag{3.13}$$

This regularization tends to preserve the divergence and the vorticity of the displaced motion field $\boldsymbol{d}$ to estimate. Nevertheless, this new term is more difficult to implement. As a matter of fact, the associated Euler-Lagrange equation is composed with two fourth-order coupled PDE's, which are tricky to solve numerically. In order to simplify the problem we have considered a modified smoothness term based on the same principles. This new smoothness term has been built by introducing auxiliary functions in the original 2^{nd} order div-curl regularization:

$$\mathcal{H}_{reg}(\boldsymbol{d}, \xi, \zeta) = \alpha \iint_{\Omega} |\mathrm{div}\boldsymbol{d} - \xi|^2 + \lambda \|\nabla \xi\|^2 + \alpha \iint_{\Omega} |\mathrm{curl}\boldsymbol{d} - \zeta|^2 + \lambda \|\nabla \zeta\|^2. \tag{3.14}$$

The new auxiliary scalar functions ξ and ζ can respectively be seen as estimates of the divergence and the vorticity of the unknown motion field, and λ is a positive parameter. The first part of each integral encourages the displacement to comply with the current divergence and vorticity estimates ξ and ζ, through a quadratic goodness-of-fit enforcement. The second part equips the divergence and the vorticity estimates with a first-order regularization favoring piece-wise smooth configurations. Getting rid of the auxiliary scalar fields ξ and ζ in (3.14) (by setting $\xi = \mathrm{div}\boldsymbol{d}$ and $\zeta = \mathrm{curl}\boldsymbol{d}$) would amount to the original *second-order* div-curl regularization (3.13).

From a computational point of view, regularizing functional (3.14) only implies the numerical resolution of first-order PDE's at the expense of course of new variables. This reformulation authorizes to use nearly the same optimization strategy involved in generic optical flow estimator. Interested readers may refer to Corpetti *et al.* (2002*b*) to get precise descriptions on the optimization strategy and on associated numerical implementation issues.

3.1.5 Minimization issue

We now turn to the minimization issue of the whole energy function $\mathcal{H} = \mathcal{H}_{obs} + \alpha\mathcal{H}_{reg}$. Two main sets of variables have to be estimated. The first one is the motion field $\boldsymbol{d}$, and the second one consists in the two scalar fields ξ and ζ. The estimation is conducted alternatively by minimizing $\mathcal{H}_{obs} + \alpha\mathcal{H}_{reg}$ with respect to $\boldsymbol{d}$, ξ and ζ:

$$\min_{\boldsymbol{h},\xi,\zeta} \mathcal{H}_{obs}(\boldsymbol{h}) + \alpha\mathcal{H}_{reg}(\boldsymbol{h}, \xi, \zeta), \tag{3.15}$$

For the motion field $\boldsymbol{d}$, the use of a robust penalty function in the observation term yields to an iteratively re-weighted least squares minimization with the estimation of outliers data z (see Appendix A.2). Concerning ξ and ζ, we have a linear least-square problem. A Gauss-Seidel solver was used for all linear least-square minimizations. The process is considered to be finished when the relative change in the L_2-norm of $\boldsymbol{h}$ is below 1%.

The minimization process is summarized below:

- $\tilde{\boldsymbol{d}} \equiv 0$
- From coarsest to finest resolution do
  - $\boldsymbol{h} \equiv 0$, $\xi \equiv 0$, $\zeta \equiv 0$, $z \equiv 0$
  - Until convergence do[a] [b] [c]

    • Estimation of $\boldsymbol{h}$ with robust functions :

$$\begin{aligned}\boldsymbol{h} \leftarrow\ & GS\Big(\iint_\Omega z(\boldsymbol{x})g^2(\boldsymbol{h}) \\ & +\alpha|\mathrm{div}\tilde{\boldsymbol{d}}(\boldsymbol{x}) + \mathrm{div}\boldsymbol{h}(\boldsymbol{x}) - \xi(\boldsymbol{x})|^2 \\ & +\alpha|\mathrm{curl}\tilde{\boldsymbol{d}}(\boldsymbol{x}) + \mathrm{curl}\boldsymbol{h}(\boldsymbol{x}) - \zeta(\boldsymbol{x})|^2 d\boldsymbol{x}\Big)\end{aligned}$$

    • Update $z(\boldsymbol{x})$ (see appendix A.2 for details):

$$z(\boldsymbol{x}) \leftarrow \tau_1 \exp -\tau_1 g^2(\boldsymbol{h})$$

    • Estimation of ξ :

$$\begin{aligned}\xi \leftarrow\ & GS\Big(\iint_\Omega |\mathrm{div}\tilde{\boldsymbol{d}}(\boldsymbol{x}) + \mathrm{div}\boldsymbol{h}(\boldsymbol{x}) - \xi - (\boldsymbol{x})|^2 \\ & +\lambda \iint_\Omega \|\boldsymbol{\nabla}(\xi(\boldsymbol{x})\|^2 d\boldsymbol{x}\Big)\end{aligned}$$

    • Estimation of ζ :

$$\begin{aligned}\zeta \leftarrow\ & GS\Big(\iint_\Omega |\mathrm{curl}\tilde{\boldsymbol{d}}(\boldsymbol{x}) + \mathrm{curl}\boldsymbol{h}(\boldsymbol{x}) - \zeta(\boldsymbol{x})|^2 \\ & +\lambda \iint_\Omega \|\boldsymbol{\nabla}\zeta(\boldsymbol{x})\|^2 d\boldsymbol{x}\Big)\end{aligned}$$

(3.16)

- If not finest resolution, pass $\tilde{\boldsymbol{d}} \leftarrow \tilde{\boldsymbol{d}} + \boldsymbol{h}$ to next resolution.
- If finest resolution, $\boldsymbol{d} \leftarrow \tilde{\boldsymbol{d}} + \boldsymbol{h}$.

---

[a] Convergence is reached when the relative change in the L_2-norm of $\boldsymbol{h}$ is below 1%.
[b] $g(\boldsymbol{h})$ denotes $\exp(\mathrm{div}\tilde{\boldsymbol{d}}(\boldsymbol{x}))\big((\tilde{E}(\boldsymbol{x})\nabla\mathrm{div}\tilde{\boldsymbol{d}}(\boldsymbol{x}) + \nabla\tilde{E}(\boldsymbol{x})) \cdot \boldsymbol{h}(\boldsymbol{x}) + \tilde{E}(\boldsymbol{x})\big) - E(\boldsymbol{x})$.
[c] "$GS()$" denotes one Gauss-Seidel iteration on the quadratic form under consideration.

Let us now have a particular attention to the minimization w.r.t the motion field $\boldsymbol{h}$ (first equation of (3.16)). For better and faster convergence, the minimization with respect to the incremental displacement field $\boldsymbol{h}$ at a given resolution is performed using the coarse-to-fine multi-parametric multigrid framework technique introduced in Mémin & Pérez (1998*b*).

More precisely, the motion is constrained to be piecewise-parametric relatively to an image partition which becomes finer and finer. At a "grid" level (named ℓ), the pixel grid is partitioned in blocks B_n^ℓ of size $2^\ell \times 2^\ell$, and the increment field is constrained to satisfy a chosen parametric model. In practice, until the penultimate grid level, the affine parametrization is chosen (i.e: $(u,v)^T = \begin{bmatrix}1 & x & y & 0 & 0 & 0\\ 0 & 0 & 0 & 1 & x & y\end{bmatrix}\Theta$). The last level $\ell = 0$ corresponds to the pixel grid itself: when it is finally reached, no parametric constraint applies anymore. At each given level, the cost terms to be minimized must be rewritten in function of the parameter vectors (Θ). This symbolic rewriting is explained in Mémin & Pérez (1998*b*). The estimation at the coarsest grid-level is fast because the space of solutions is of reduced dimension. It serves as a reliable initialization for the next level, yielding to this new computation more efficiency , and so on until the pixel

grid itself. The combination of the multiresolution and the multigrid techniques partly makes possible to prevent from stopping the process of minimization in a local minimum. More details of the minimization issues can be seen in Corpetti *et al.* (2002*b*).

3.2 Variational Motion Estimation for Incompressible Flows

The optical flow presented in this section was proposed by the CVGPR group (Yuan *et al.*, 2005, for more details).

The variational optical-flow based methods give us the following minimization problems

$$\min_{u} \|g_1(x+u) - g_2\|^2 + \mathrm{Reg}(u;\ \lambda); \tag{3.17}$$

where in this work the high-order regularization term $\mathrm{Reg}(u;\ \lambda)$ is given:

$$\mathrm{Reg}(u;\ \lambda) = \lambda_1 \|\nabla \operatorname{div} u\|^2 + \lambda_2 \|\nabla \operatorname{curl} u\|^2 + \lambda_3 \|\partial_n u_n\|^2 . \tag{3.18}$$

Here the first term penalizes the smoothness of divergence field and the second penalizes the variance of curl field. The last term regularizes the smoothing boundary flows which is important for the numerical stabilities. For the 2D divergence-free flows, the motion field u can be simply expressed by

$$u \ = \ \nabla^{\perp}\psi.$$

and the penalties for variance of divergence, i.e.$\|\nabla \operatorname{div} u\|^2$, in the regularization terms is simply droped out. Hence the optimization problem (3.17) is reduced into

$$\min_{\psi} \left\|g_1(x+\nabla^{\perp}\psi) - g_2\right\|^2 + \lambda_1 \|\nabla \triangle \psi\|^2 + \lambda_2 \left\|\partial_n (\nabla^{\perp}\psi)_n\right\|^2 \tag{3.19}$$

where velocity estimation is based on one scalar potential field ψ. In order to keep the incompressible condition, the mimetic finite difference method is used to formulate the estimation problem in finite dimensional space (see Fig. 3.1). In the correspondent discrete expression, the velocity field can be represented:

$$u = \mathbb{G}^{\perp}\psi, \quad u \in H_S, \ \ \psi \in H_P$$

where $H_{P,V,S,E}$ are related discrete function spaces which are well defined in the mimetic finite difference method. And the minimization problem is written as:

$$\min_{\psi} \left\|I_1(x+\mathbb{G}^{\perp}\psi) - I_2(x)\right\|_{H_V}^2 + \lambda_2 \|\mathbb{G}\triangle_C \psi\|_{H_E}^2 + \lambda_3 \left\|\mathbb{P}\ \mathbb{G}^{\perp}\psi\right\|_{bc}^2 \tag{3.20}$$

where the respective matrix $\mathbb{P}$ presents the operator ∂_n in last regularization term and $\|\cdot\|_{bc}$ is the norm evaluating elements along the boundary. The advantages of such discrete incompressible expression is that we can reduce nearly half the number of unknown values and at the same time the divergence-free condition is well kept implicitly.

In practice, a multi-level computation framework is implemented in order to capture the large displacements. Two image pyramids $\{I_i^l\}_{l=1,\ldots,m}$, $i = 1, 2$, are constructed. $l = 0$ denotes the original image, and $l = m$ denotes the coarsest level. At level l, given potential fields $\tilde{\psi}^l$, and the velocity field $\tilde{u}^l = \mathbb{G}^{\perp}\tilde{\psi}^l$, image I_2^l is warped to $\tilde{I}_2^l = I_2^l(x - \tilde{u}^l)$. The image flow between the two images $\tilde{I}_1^l$ and I_2^l is assumed to be small enough to allow for accurate linearization:

$$\partial_t I^l = I_1^l - \tilde{I}_2^l \tag{3.21}$$

$$\Delta_u^l = \mathbb{G}^* I_1^l \cdot (u^l - \tilde{u}^l) \tag{3.22}$$

$$\Delta_\psi^l = \mathbb{G}^* I_1^l \cdot (\mathbb{G}^{\perp}(\psi^l - \tilde{\psi}^l)). \tag{3.23}$$

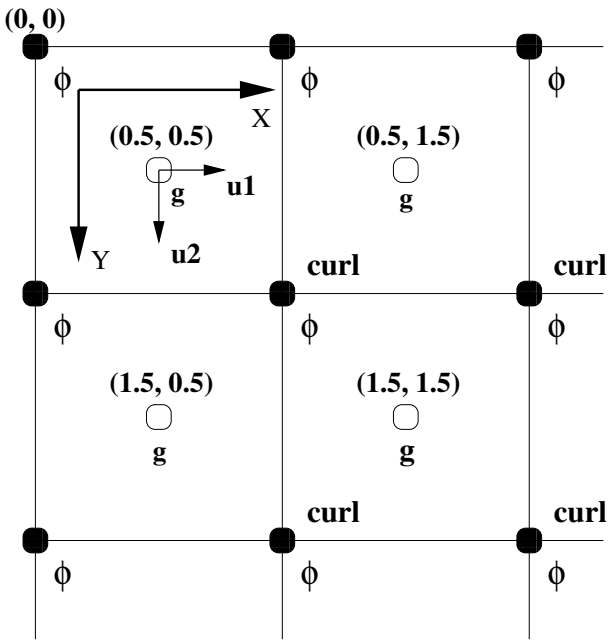

Figure 3.1: Definition of finite-dimensional spaces of scalar fields and vector fields on a square grid. Filled circles depict *nodes* or *vertices*, the other circles indicate *cells*. The positions of diamonds are referred to as *sides*.

The residual motion field u^l, in terms of $\mathbb{G}^{\perp}\psi^l$, is estimated by solving the problem

$$\min_{\psi^l} = \left\|\Delta^l_{\psi} + \partial_t I^l\right\|^2_{H_V} + \lambda_2 \left\|\mathbb{G}\triangle_C \psi^l\right\|^2_{H_E} + \lambda_3 \left\|\mathbb{P}\,\mathbb{G}^{\perp}\psi^l\right\|^2_{bc} \tag{3.24}$$

The minimizer ψ^l and u^l are postprocessed to yield the initialization $\tilde{\psi}^{l-1}$and $\tilde{u}^{l-1}$ of the next finer level $l-1$. The whole process is started at the coarsest level m with $\tilde{\psi}^m = 0$ and $\tilde{u}^m = 0$, and looped until the finest level $l = 0$.

3.3 Collaborative scheme for robust optical flow estimation

In this section, we propose to design a novel approach that combine the robustness of correlation techniques with the high density of the global variational methods presented in §3.1. This results in a technique that is robust under noise and outliers, while providing a dense motion field. This new method was proposed by INRIA and validated in collaboration with Cemagref (Héas *et al.*, 2007; Heitz *et al.*, 2007).

3.3.1 Classical method

A clasical approach used with PIV imagery is correlation-based matching, which corresponds to the DFD constraint (see §3.3.2) associated to a locally constant field within a neighborhoods $W(\mathbf{s})$. Thus, using a discrete space of vectors $\{\mathbf{w}\}$, the velocity $\mathbf{u}$ at point $\mathbf{s}$ is obtained as

$$\mathbf{u}(\mathbf{s}) = \arg\min_{\mathbf{w}} \sum_{\mathbf{r}\in W(\mathbf{s})} \mathcal{C}(I(\mathbf{r}+\mathbf{w}, t+1), I(\mathbf{s}, t)), \tag{3.25}$$

where $\mathcal{C}(.)$ denotes a dissimilarity function. On one hand, these approaches suffer from several deficiencies : traceable features must be sufficiently contrasted and must persist over time on consecutive images. Furthermore, the estimation prone to erroneous spatial variability, which can be reduced with the use of filters. On the other hand, these techniques constitute very fast

methods and are generally locally very robust to noise. These techniques are based on disjoint local estimation, and thus produce sparse vector fields estimated locally and independently.

3.3.2 Fluid dedicated optical flow method

The apparent motion, perceived through variations of image intensity I is called *optical flow* in the computer vision community. All optical flow estimation methods rely on the temporal conservation of some invariants. The most common are photometric invariant which can easily be extracted and may lead to dense measurements. In the case of PIV imagery for bi-dimensional flows visualization, the gray level constancy assumption can be assumed, leading to an integrated non-linear formulation called the Displaced Frame Difference (DFD) equation $I(\mathbf{s}+\mathbf{u}(\mathbf{s}), t+1) = I(\mathbf{s}, t)$, or at time t, to a linear differential formulation called the Optical Flow Constraint (OFC) equation $\mathbf{u}(\mathbf{s}).\nabla I(\mathbf{s}) + I_t(\mathbf{s}) = 0$, where $\mathbf{s}$ denotes the spatial coordinates (x, y) and $\mathbf{u}(\mathbf{s})$ the apparent motion field at this point and at a given time t.

These two formulations can not be used alone, as they provide only one equation for two unknowns at each spatio-temporal location $(\mathbf{s}, t)$. This is the well known *aperture problem* where the so called *normal flow* to the brightness gradient is estimated while the tangential velocity component remains undetermined. In order to remove this ambiguity and robustify the estimation, one must rely on other assumptions. The main used assumption is *local* spatial or spatio-temporal constancy of the velocity fields (Lucas & Kanade, 1981; Bigün & Granlund, 1988).

Alternate approaches, derived in the framework proposed by Horn & Schunck (1981*b*), have the great advantage of producing dense vector fields with spatial *global coherence*. They are based on the minimization of an energy function $J = J_d + J_r$ composed of two terms. The first term J_d is called the data term and implements the OFC equation

$$J_d(\mathbf{u}, I) = \int_\Omega \phi[\nabla I(\mathbf{s}).\mathbf{u}(\mathbf{s}) + \frac{\partial I(\mathbf{s})}{\partial t}]d\mathbf{s}. \tag{3.26}$$

The penalty function ϕ is usually the L_2 norm but it may be changed to a robust function attenuating the effect of data that deviate significantly from the OFC (Black & Anandan, 1996). The second term J_r is called the regularization term. It is usually a standard first-order spatial smoothness term

$$J_r(\mathbf{u}) = \alpha \int_\Omega \phi(\| \nabla \mathbf{u} \|)d\mathbf{s}, \tag{3.27}$$

where $\alpha > 0$ is a parameter controlling the balance between the smoothness and the global adequacy to the brightness constancy assumption. Function ϕ may be the quadratic penalty if the searched solution is smooth everywhere or a robust norm function if one wants to handle implicitly the spatial discontinuities of the field (Black & Anandan, 1996). However in the case of fluid flows, it can be demonstrated that a first order regularization is not adapted as it favors the estimation of velocity fields with low vorticity. A second order regularization can advantageously be consider as proposed in (Suter, 1994*b*) :

$$J_r(\mathbf{u}) = \alpha \int_\Omega \phi(\| \nabla \xi(\mathbf{s}) \|^2 + \| \nabla \zeta(\mathbf{s}) \|^2)d\mathbf{s}, \tag{3.28}$$

where $\xi = curl\mathbf{u} = \frac{\partial u}{\partial y} - \frac{\partial v}{\partial x}$ and $\zeta = div\mathbf{u} = \frac{\partial u}{\partial x} + \frac{\partial v}{\partial y}$ stand for the vorticity and divergence of the apparent velocity $\mathbf{u} = (u, v)^T$. Note that in the case of bi-dimensional incompressible flows, divergence of the apparent motion is equal to zero. To circumvent the difficulty of implementing second order smoothness constraint, this regularization term can be simplified in a computational point of view in two interleaved first-order div-curl regularizations based on an auxiliary variable ξ_1 and $\zeta_1$approximating the vorticity and the divergence of the flow (Corpetti *et al.*, 2002*a*, 2006). Thus we have :

$$J_r(\mathbf{u}) = \alpha \int_\Omega \phi[(\xi(\mathbf{s}) - \xi_1)^2 + \lambda \parallel \nabla\xi_1 \parallel^2] d\mathbf{s} \tag{3.29}$$

$$+\alpha \int_\Omega \phi[(\zeta(\mathbf{s}) - \zeta_1)^2 + \lambda \parallel \nabla\zeta_1 \parallel^2] d\mathbf{s}, \tag{3.30}$$

where λ is a positive regularization parameter.

3.3.3 Multiresolution approach

However, one major problem with optical flow estimators is large displacement estimation. The intensity function must be locally sufficiently close to a linear function. Since the larger the displacement the more narrow the linearity domain is, large displacements can not be recovered directly. A common way to overcome this limitation is to create a image pyramid, constructed by successive low-pass filtering and down sampling of the original images. In this framework, principal components of displacements are first estimated at coarse resolution where motion amplitude should be sufficiently reduced in order to satisfy the linearity requirement. Incremental displacement are then estimated while going down the pyramid, and the solution is refined (Bergen *et al.*, 1992). However, since the multiresolution schemes estimates principal component displacements only at coarse resolutions where small structures are rubbed out, this approach enables the characterization of large displacements of small structures only in the case when their motion are close enough to the principal component's one. Another disadvantage characterizing the method is the additional noise incorporation due to the calculation of motion-compensated images at each resolution by the use of interpolation methods.

3.3.4 Collaborative correlation-optical flow scheme

To overcome the multiresolution limitations, we propose an alternative approach relying on a unique representation of the full resolution image. Thus, the proposed method tackles the non-linear estimation problem without making successive approximations in the calculation of interpolated images nor restricting itself to the characterization of large displacements of sufficiently large structures. The proposed method takes advantage of the non-linear formulation of the motion estimation problem within a differential framework appropriated for globalized local smoothings. More explicitly, large displacements of both, fine or large structures, can be recovered by correlation-based methods for sufficiently contrasted and persisting image regions. Thus, the idea of the method is to replace the coarse estimates of the multiresolution scheme by a dense large scale displacement estimate derived from a collection of correlation-based vectors $\mathbf{u}_c$ obtained by Eq.3.25.

A new functional was defined to estimate de vector fields

$$J(\mathbf{u}) = J_d(I, \mathbf{u}) + J_r(\mathbf{u}) + J_c(\mathbf{u}, \mathbf{u}_c), \tag{3.31}$$

where $J_c(.)$ is the energy function constraining estimated displacements $\mathbf{u}$ to be close to a sparse correlation-based vector field $\mathbf{u}_c$. Thus, functional $J_c(.)$ is defined as a quadratic distance between the solution and a collection of correlation-based vectors $\mathbf{u}_c^i = (u^i, v^i)$ located at the point $\mathbf{s}^i = (x^i, y^i)$ and influencing their neighborhood according to a bi-dimensional Gaussian $\mathcal{N}^i(\mathbf{s})$ of mean $\mathbf{s}^i$ and of variance σ

$$J_c(\mathbf{u}, \mathbf{u}_c) = \gamma \int_\Omega \sum_{i=1}^{L} g^i \mathcal{N}^i(\mathbf{s}) \parallel \mathbf{u}_c^i - \mathbf{u}(\mathbf{s}) \parallel^2 d\mathbf{s}, \tag{3.32}$$

where g^i and γ denote respectively the confidence and the functional weighting factors.

Chapter 4

Results

This chapter describes the results obtained for the evaluation of OF1 approach §4.1, OF2 approach §4.2 and COROF1 approach §4.3.

4.1 Dense estimation with fluid dedicated optical flow

This section presents the results obtained for OF1 approach with data images already available at the beginning of the project FLUID (the VSJ standard images §4.1.1, the mixing layer §4.1.2 and the near wake of a circular cylinder §4.1.3), with the images of the PIV Challenge 2005 (see §4.1.4) and with the first set of images of the FLUID project database (see §2.5 and §2.6).

4.1.1 Results for the VSJ standard images

Figure 4.1 shows the average L_1 relative error of 6 algorithms: **A1**, the Orthogonal Dynamic Programming (ODP) issued from Quénot (1999); **A2**, the Variational Optical Flow (VOF) implementation of Horn & Schunck presented in Ruhnau *et al.* (2005); **A3**, the robust multiresolution/multigrid (RMM) implementation of Horn & Schunck presented in Mémin & Pérez (1998*a*); **A4**, the proposed approach; **A5**, the proposed Integrated Continuity Equation (ICE) associated to a first order regularization and **A6**, the usual OFCE constraint associated to the presented Div-Curl regularization.

Compared to other methods the proposed approach gives better results for cases #1, #2, #5, #6, #7, #8. Results on case #4 are good for all techniques, with slightly better results for estimators **A1** and **A2**. Nevertheless, as expected, the div-curl and ICE options (**A4**) are better than others combinations (**A3**, **A5** and **A6**) with the same implementation method. Concerning case #3 (where the motion range is low), all estimators give important errors on the motion field. The bad results obtained with the proposed technique can be explained by *i)* the multiresolution process (which introduces errors due to bilinear interpolation and was not necessary in this case); *ii)* by the div-curl regularization (which seems to introduce more artifacts than the others methods) and *iii)* by the ICE constraint (the out of plane velocity is very small here and this option is likely to introduce a divergent motion at each change of illumination). Nevertheless, in practice, it is often possible to have an idea of the magnitude of the motion and to adapt the parameters. Case #2 is very interesting: referring to table 2.1, one can see that the velocity is very important (and as a consequence, the underlying vorticity too). Even if most of the presented approaches have a multiresolution implementation, all estimators equipped with a first order regularization seem to smooth the higher value of the curl and the div, yielding to high errors. Conversely, estimators with a div-curl smoothing (**A4** and **A6**) give reliable results. The results on the important out-of-plane velocity in case #8 confirm that the proposed ICE is a correct choice. On this eight synthetic examples, the proposed method gives better results. We now turn to comparisons on two different types of real image sequences and

compare our method with a classical PIV system.

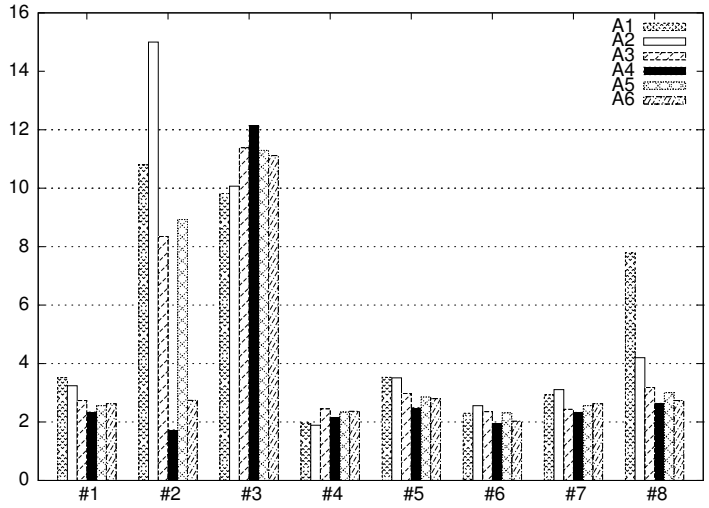

Figure 4.1: Average relative L_1 error of 6 algorithms. From left to right (and top to bottom in the legend): **A1:** ODP from Quénot (1999); **A2:** VOF from Ruhnau *et al.* (2005); **A3:** RMM from Mémin & Pérez (1998*a*); **A4:** The proposed approach OF1; **A5:** The proposed ICE associated to a first order regularization and **A6:** The usual OFCE associated to the presented Div-Curl regularization.

4.1.2 Results for the mixing layer

Instantaneous velocity field

Images of the same instantaneous vector field are shown in figure 4.2-(a) and in figure 4.3-(a), for Optical-flow and PIV approach, respectively. Only one vector out of two hundred and twenty five were represented for Optical-flow. Results exhibit the footprint of the primary structures of the mixing layer. Based on vector fields both approaches gave comparable information but with higher density for Optical-flow. Figure 4.2-(b) and 4.3-(b) show contours of constant spanwise vorticity $\omega_z^\star$. When compared with PIV results, Optical-flow approach exhibited more localized information. Nevertheless, vorticity yielded more noisy contours and higher levels of vorticity. As mentioned in section 4.1.2, it might be possible that this noisy vorticity was due to the measurement noise in the input images.

Mean quantities

In a mixing layer, the mean streamwise velocity component can be expressed with the theoretical solution as:

$$\frac{\overline{U} - U_b}{U_a - U_b} = \frac{1}{2}(1 - \mathrm{erf}(\sigma\eta)), \tag{4.1}$$

where $\eta = (y - y_o)/(x - x_o)$ with (x_o, y_o) the coordinate of the virtual origin of the mixing layer and where the spreading parameter σ is constant.

For each streamwise location x and for both approaches the experimental values fitted the theoretical solution. Results gathered in table 4.1 show that the spreading parameter σ adjusted from Optical-flow and PIV treatment was of the order of 49.8 and 43.6, respectively. Optical-flow value compared well with the value of 52.7 obtain by Heitz (1999) with pitot tube measurements, while PIV gave poor agreement. For both approaches, the evolution of the vorticity thickness δ_ω, defined as $\delta_\omega = -\Delta U/(\partial U/\partial y)_{\max}$ where $\Delta U = U_a - U_b$, supported the observation of

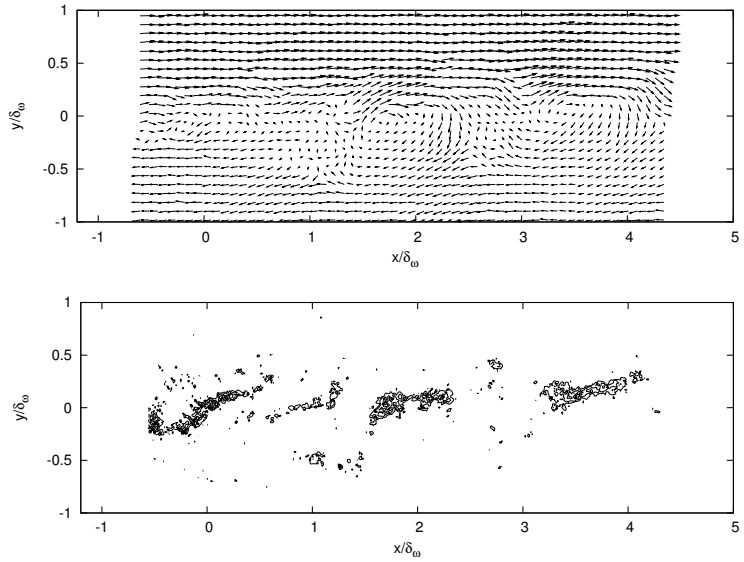

Figure 4.2: Views of instantaneous turbulent plane mixing layer structure at $Re_{\delta_\omega} = 7000$. Optical-flow: Top, Instantaneous vector field (one vector out of 225); Bottom, Instantaneous spanwise isocontour of vorticity $\omega_z^\star = (\omega_z \Delta U)/\delta_\omega$ ($\omega^\star_{z_{\min}} = -9$, $\omega^\star_{z_{\max}} = -2$, $\Delta\omega_z^\star = 1$).

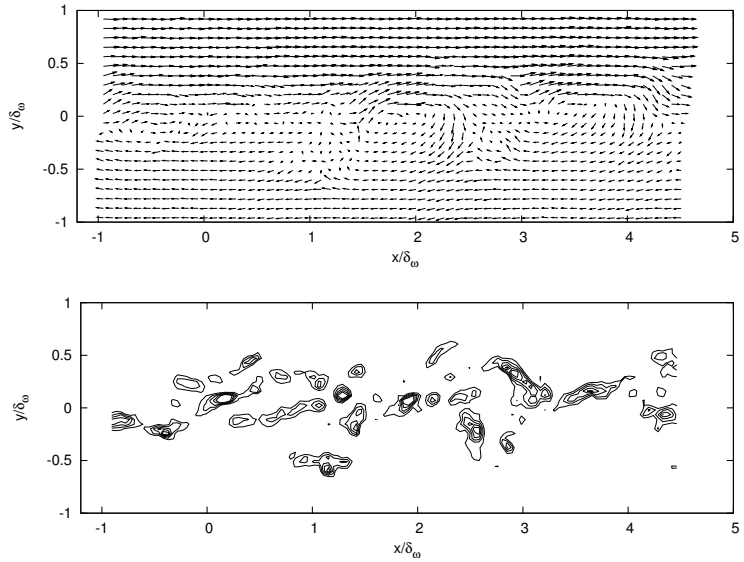

Figure 4.3: Views of instantaneous turbulent plane mixing layer structure at $Re_{\delta_\omega} = 7000$. PIV - multipass 32-16 treatment: Top, Instantaneous vector field (one vector out of nine); Bottom, Instantaneous spanwise isocontour of vorticity $\omega_z^\star = (\omega_z \Delta U)/\delta_\omega$ ($\omega^\star_{z_{\min}} = -9$, $\omega^\star_{z_{\max}} = -2$, $\Delta\omega_z^\star = 1$).

a linear growth of the mixing layer. As for the spreading parameter, PIV results exhibited a higher growth of the mixing layer. This behaviour can be explained by the interrogation interval in which the velocity estimated was an average value, in a region where there were high displacements gradients.

	Heitz (1999)	PIV	optical-flow
r	0.67	0.67	0.67
λ	0.2	0.2	0.2
σ	52.7	43.55	46.37
$d\delta_w/dx$	0.0336	0.0407	0.0382

Table 4.1: Comparison on main characteristics parameters of the mixing layer for Pitot-tube measurements (Heitz (1999)), PIV and Optical-flow approaches

To have a finer analysis, it is of primary interest to observe the superior order moments. To that end, the distribution of the Reynolds stress are represented in figure 4.4. Data were compared with Heitz (1999) fourth hot-wire measurements. Results show that PIV approach gave a slight overestimation of $\overline{u'^2}$ and $\overline{u'v'}$ and a slight underestimation of $\overline{v'^2}$. Optical-flow approach better fitted hot-wire measurements.

It should be noted that for PIV and Optical-flow approaches the second order moments were computed with 520 samples, hence the Reynolds stress were not statistically converged values, whereas for hot-wire measurements more than 100000 samples were collected. As a consequence, we can say that both PIV and Optical-flow approaches gave similar results in good agreement with the litterature.

Discussions of results

This first experience proved the ability of the OF1 method to recover dense motion fields from PIV images. Main characteristics of the flow (mixing layer mean characteristics and second order moments) were recovered in a similar way with both approaches (PIV and the proposed Optical-flow). A major difference between the two approaches was the number of vectors that the Optical-flow technique was able to extract. Furthermore, it should be noted that Optical-flow approach was able to extract more information (e.g. noisy) contained in the image than PIV approach did. Let us nevertheless remark that, from a time computation point of view, the presented method took nearly 120 s for the estimation of an instantaneous dense motion field on a PC-linux (2.8GHz, 1.5Go-RAM) whereas the estimation with the PIV approach based on cross-correlation took only 15 s. Some interrogations came also about the level of the noise obtained in the vorticity fields from the Optical-flow method.

4.1.3 Results in the near wake of a circular cylinder at Re=3000

Instantaneous velocity field

Instantaneous velocity field and vorticity contours are shown in figures 4.5 and 4.6 for the proposed Optical-flow approach and for the PIV approach, respectively.

The motion fields obtained from the two methods were very similar and correctly represented the physical phenomenon. Indeed, the main vortex launched in the middle of the image appears clearly in the velocity field as well as in iso-vorticity contours. In figures 4.5 and 4.6, these contours are very interesting to analyze. Indeed, it can be observed that both shared the main phenomena but that the major difference appeared in the spatial resolution, that of the optical flow approach being highly superior. This led to a better topological description of the near wake flow. Nevertheless, a more precise study on this over-information must be carried out to reach its relevance. A work on that subject is currently in progress. Let us notice, as we

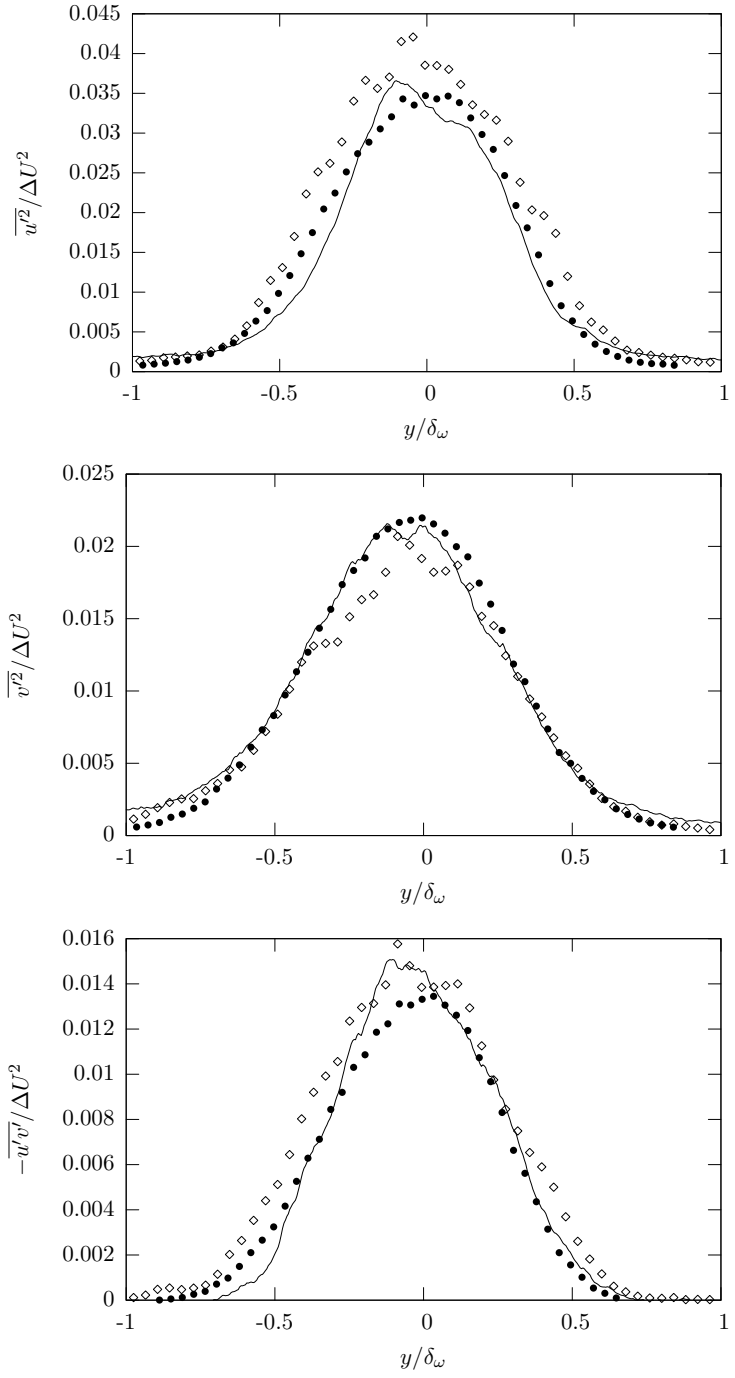

Figure 4.4: Reynolds stress distributions of the mixing layer at $x/\delta_\omega = 4$. Each symbol representing a velocity measurement technique: −, Optical-flow; ◇, PIV; •, Hot-wire (Heitz, 1999).

previously mentioned, that the higher quality of the input images used for this experiment (a 12 bit CCD Pelletier cooled camera vs a 8 bit one for the mixing layer) was probably responsible of the better results, in term of noise, of the vorticity map issued form the optical-flow velocity field.

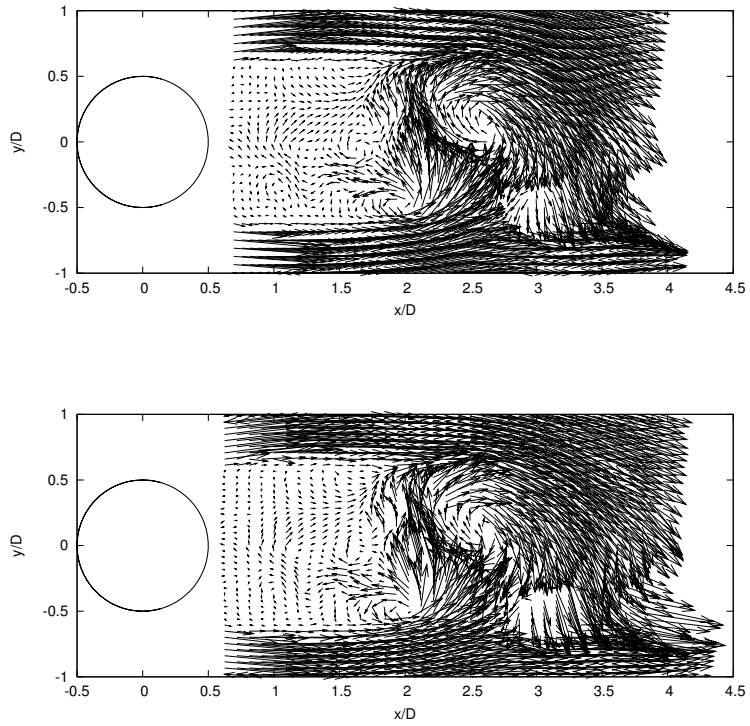

Figure 4.5: View of instantaneous near wake vector field at Re=3000: Top, Optical-flow treatment (1 vector out of 256); Bottom, PIV treatment (1 vector out of 4).

Mean quantities

In this section, all motion fields from the 540 pairs of images of the whole sequence were computed. For both methods, mean velocity fields and their corresponding streamlines are represented in figures 4.7 a and 4.7 b, respectively.

At values of x/D greater than 1.5, the patterns of isocontours of the mean streamwise velocity remained roughly the same. At smaller values of x/D, the velocity pattern exhibits, however, slight differences in the description of the shear layers. Indeed, the same isovalue of the mean streamwise velocity, indicated a larger thickness of the shear layers with the Optical-flow approach than with PIV. From the patterns of isocontours of the transverse mean velocity, represented in figures 4.7 and 4.7, it appeared that results obtained with Optical-flow approach were smoother than with PIV. This indicated that with the same number of samples, or data images, the statistical quantities exhibited more converged values with Optical-flow than with PIV. In figure 4.8, this behaviour was readily observed with second order moments, which converge later than first order moments. Furthermore, these smoother results were associated with a better symmetry across the wake centreline. These differences can be explained by the global regularization methods which is involved in the proposed algorithm and leads to homogeneous results, compared to PIV which is a local approach giving a mean value to each considered area.

The better representation of the patterns of the mean quantities gives a better location of

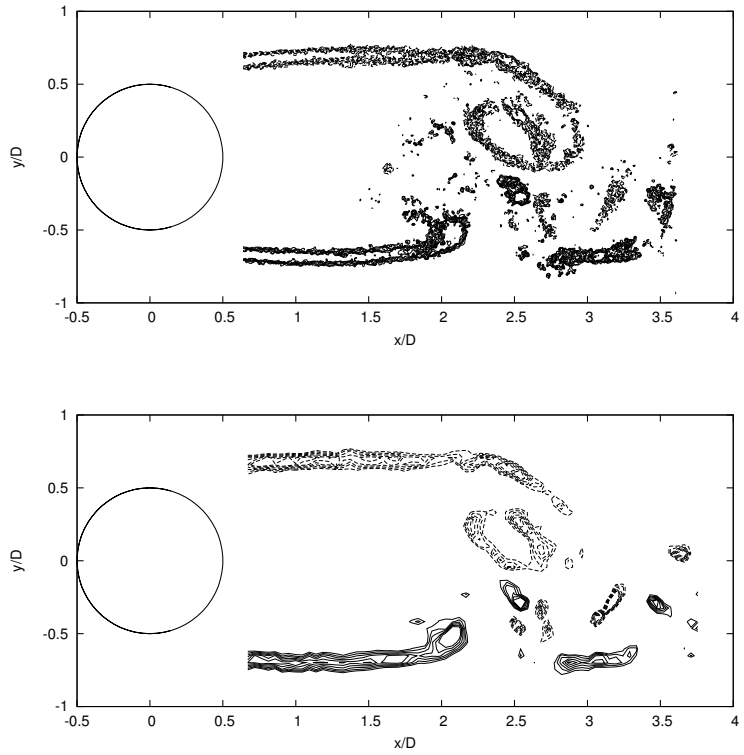

Figure 4.6: View of instantaneous near wake iso-contour of vorticity at Re=3000 – $\omega_z^\star = (\omega_z U)/D$ ($|\omega_{z_{min}}^\star| = 0.5$, $|\omega_{z_{max}}^\star| = 10$, $\Delta\omega_z^\star = 1$): Top, Optical-flow treatment; Bottom, PIV treatment.

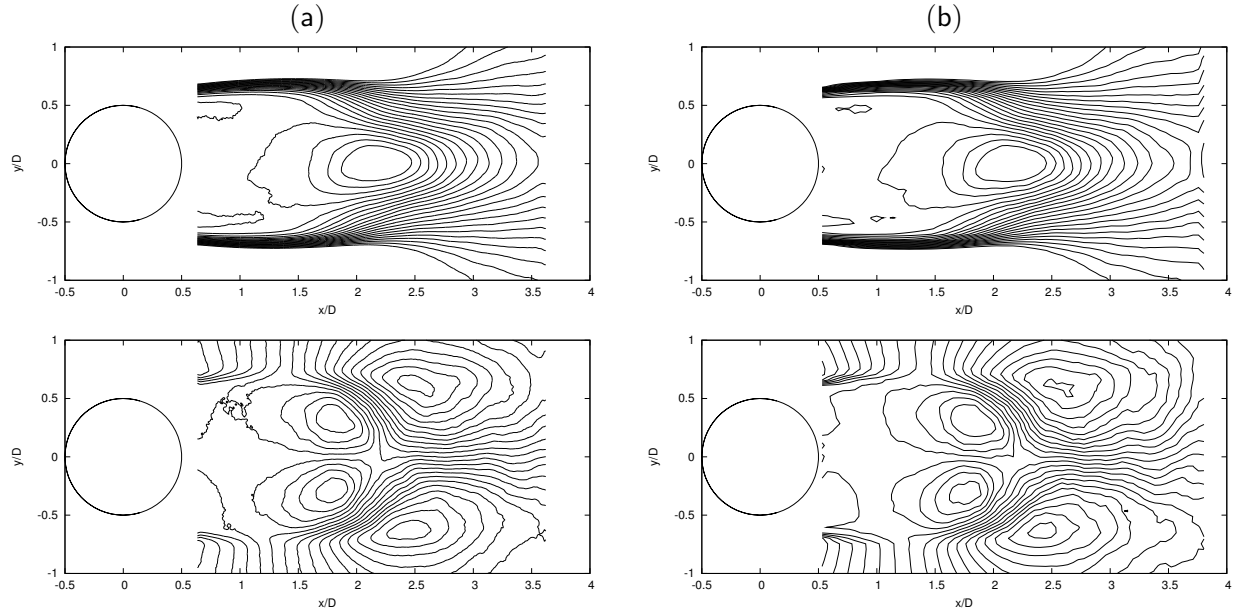

Figure 4.7: From top to bottom, 21 iso-contours of mean streamwise velocity $U/U_\infty = -0.2, ..., 1$ and of mean transverse velocity $V/U_\infty = -0.25, ..., 0.25$: (a), Optical-Flow measurements; (b), PIV measurements.

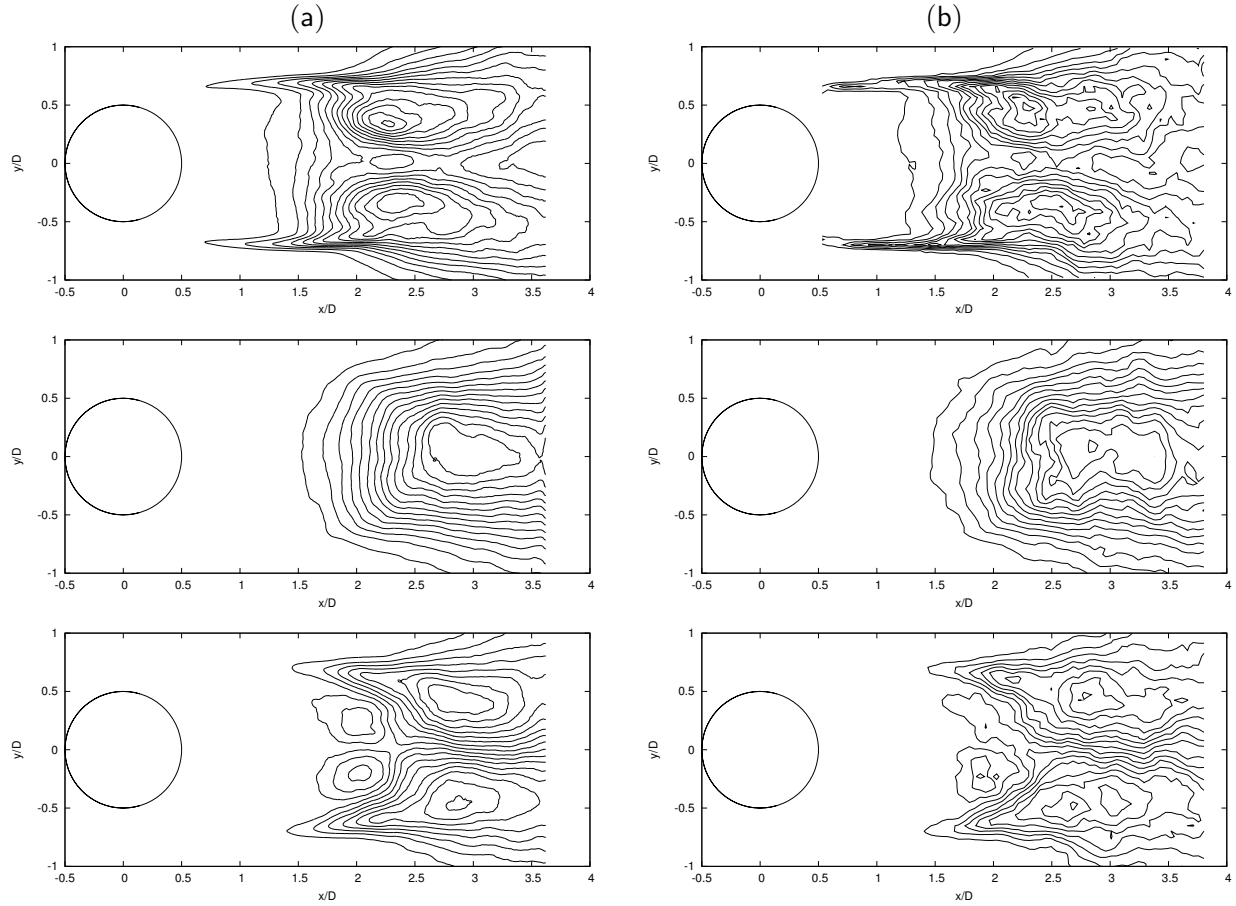

Figure 4.8: From top to bottom, 15 iso-contours of $\overline{u'^2}/U_\infty^2 = 0, ..., 0.05$, $\overline{v'^2}/U_\infty^2 = 0, ..., 0.1$ and $\overline{u'v'}/U_\infty^2 = -0.025, ..., 0.025$: (a), Optical-Flow measurements; (b), PIV measurements.

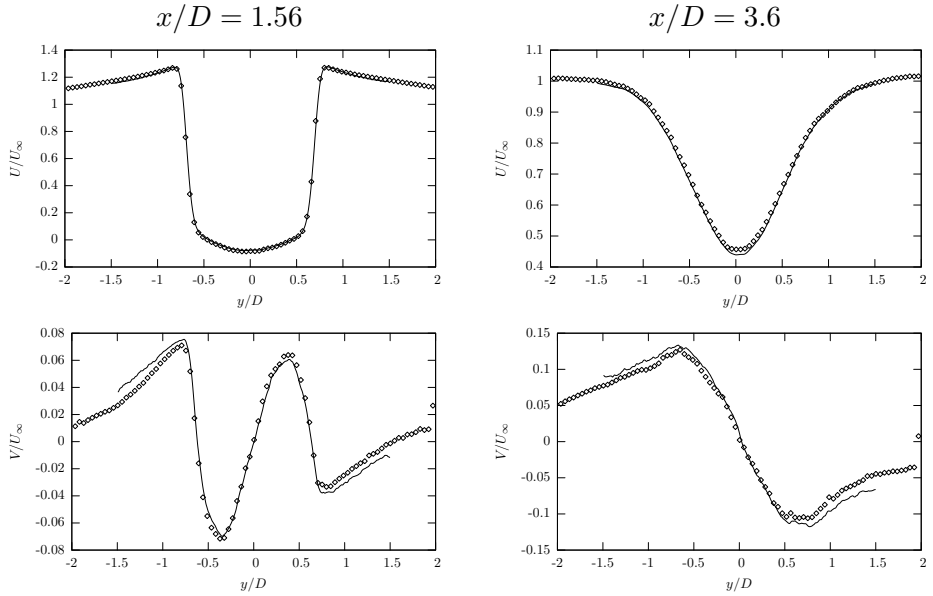

Figure 4.9: Comparison of profiles of mean velocity components U and V at two locations downstream of the cylinder: –, Optical-Flow measurements; ⋄, PIV measurements.

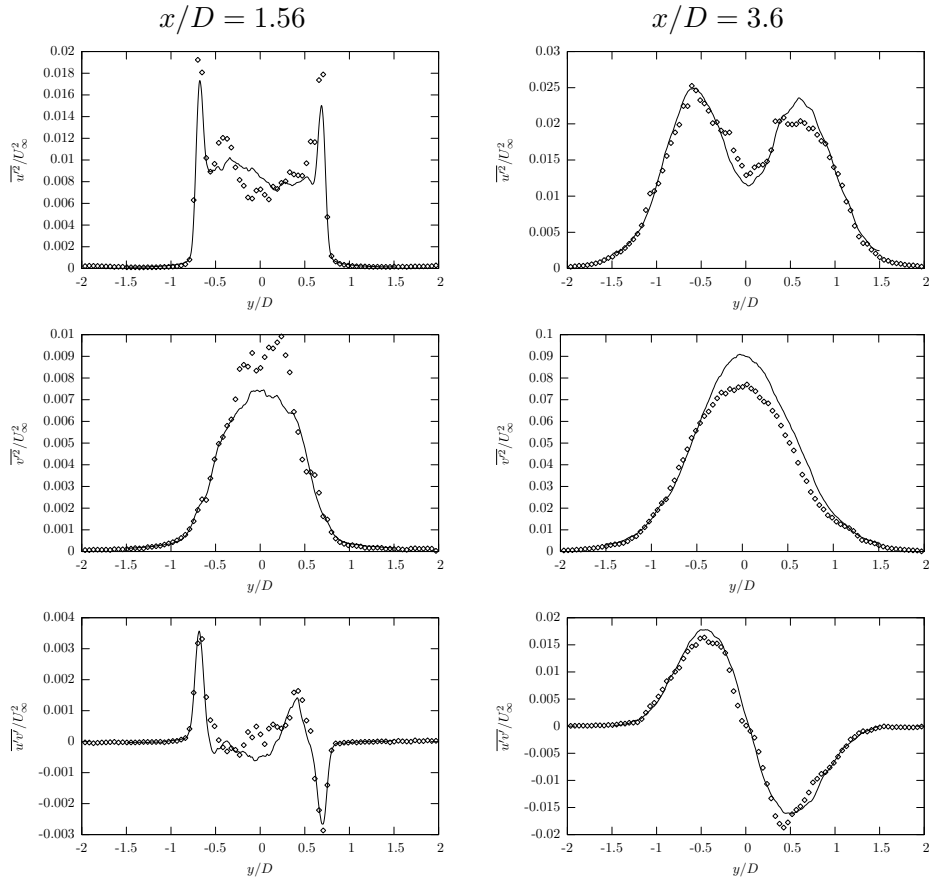

Figure 4.10: Comparison of profiles of Reynolds stresses at two locations downstream of a cylinder: –, Optical-Flow measurements; ⋄, PIV measurements.

the different maxima of $\overline{u'^2}$ and $\overline{v'^2}$ which are characteristics of the vortex formation region. Two main approaches can be distinguished to extract the streamwise length of the recirculation region: the distance between the base of the cylinder and the point with null longitudinal mean velocity ($U = 0$) on the centreline of the flow ($y = 0$), called the bubble length (L_R), and the distance to the point where the ($\overline{u'^2} + \overline{v'^2}$) quantity is maximum on the centreline, called the formation length (L_f). The latter criterion defined by Bloor & Gerrard (1966) enables to compare results with single hot-wire cooling velocity measurements. Single hot-wire measurements were carried out with the wire parallel to the axis of the cylinder $y-$axis, so that measurements were more sensitive to the cross-flow induced by the formation of the Kármán vortices. Critical values along the wake centreline are presented in table 4.2. Results show that the bubble length was nearly the same for Optical-flow and PIV methods, whereas the formation length was better determined with the former approach, close to hot-wire measurements, than with the latter one. Presumably, this may be related to the better extraction, with Optical-flow schemes, of the vortices formed and launched in the very near wake, as it is shown in figure 4.6. It should be noticed that, due to the low aspect ratio ($L/D = 14.2$ without end plates), the critical values along the wake centreline yielded larger mean longitudinal velocity minimum and formation length than those observed when the aspect ratio was sufficiently large to be independent of this parameter.

To have a quantitative idea of the relevance of different results, we represent in figure 4.9 and 4.10 mean velocity and Reynolds stress profiles at two locations downstream of the cylinder ($x/D = 1.56$ and $x/D = 3.6$). For both algorithms, mean velocity distributions were in good agreement. Concerning Reynolds stress, the shape of all curves were quite similar. However, their local extrema were different. For $x/D = 1.56$, optical-flow underestimated the fluctuating velocity levels compared to PIV. Let us recall that this region corresponds to the free shear layers spreading, which for the subcritical regime concerned, exhibits small vorticity thicknesses with large gradients. The proposed algorithm, which is based on a global regularization, uses a quadratic smoothness constraint $\mathcal{H}_{reg}$ which enforces a spatial smoothness of the divergence and the vorticity of the motion field. This may explain the lower value of each extremum provided by the optical-flow estimator. Further improvements could be obtained using a robust penalty function Ψ_2 is the second part of the regularization term of equation (3.14) :

$$\alpha \iint_{\Omega} |\mathrm{div}\boldsymbol{d} - \xi|^2 + \lambda\Psi_2(\|\boldsymbol{\nabla}\xi\|) + \alpha \iint_{\Omega} |\mathrm{curl}\boldsymbol{d} - \zeta|^2 + \lambda\Psi_2(\|\boldsymbol{\nabla}\zeta\|)$$

Such a penalty term should be able to obtain better estimates of the motion fields and in particular to extract better local extrema of the Reynolds stress. Nevertheless, this form yields to the definition of an other threshold parameter. In order to quantify the effect of a robust penalty function, new research studies with dedicated experiments are currently in progress in our laboratories. For $x/D = 3.6$, the differences between the two approaches were consistent with the distinct estimation of the recirculation region, seen above for the formation length.

	Hot-wire	PIV	Optical-flow
$U_{\min}/U_\infty$	-	-0.30	-0.29
L_R/D	-	2.70	2.73
L_f/D	2.80	2.71	2.85

Table 4.2: Critical values along the wake centreline, $y = 0$.

4.1.4 PIV Challenge 2005

The Cemagref in collaboration with INRIA have submitted a dense optical flow method dedicated to fluid flows to the PIV challenge 2005. This challenge which aims at comparing different

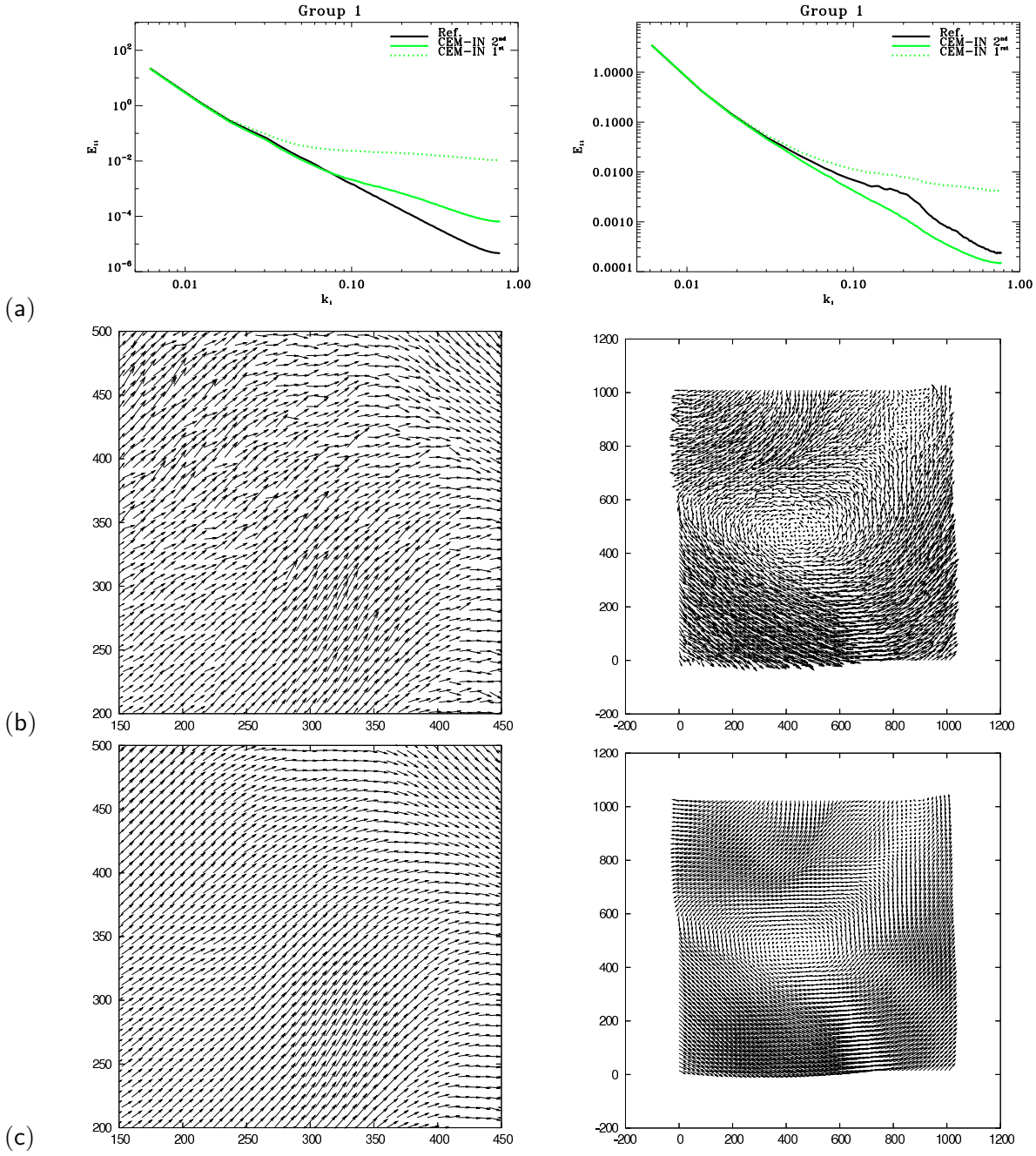

Figure 4.11: PIV Challenge 2005: (left), case A2 from M. Stanislas (synthetic turbulence with spectrum slope equal to -3); (right), case A3 from Stanislas (stratified flow simulation). Results obtained with a fluid dedicated dense motion estimator (OF1) for two extreme tuning of regularization parameters: (a), spectrum of the velocity; (b), velocity fields corresponding to the spectrum with the green dashed line; (c), velocity fields corresponding to the spectrum with the green line. The spectrum in black is the reference.

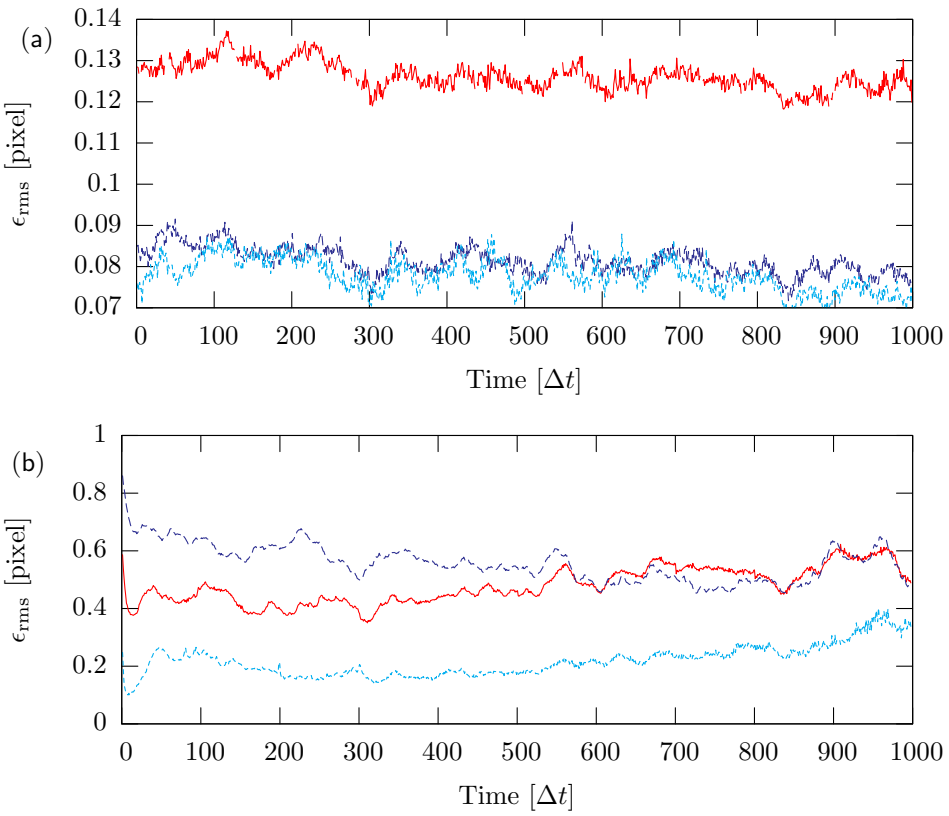

Figure 4.12: RMS of the error of the U velocity component extracted from (a), images of particles dispersed in 2D turbulence (case C1a); (b), images of scalar dispersed in 2D turbulence (case C1b). Red, OF1 approach; blue, correlation technique; light-blue; OF2 approach.

motion estimator for images of fluid flows seeded with particle held in Pasadena, California in September 2005. The dense motion estimator was able for two extreme tuning of the algorithm parameters to give good results for most of the different benchmarks focussing on the assessment of the spatial resolution. Figure 4.11 shows results obtained for two extreme tuning of regularization parameters in a synthetic turbulence with spectrum slope egal to -3 (PIVChallenge case A2) and in a stratified flow simulation (PIVChallenge case A3). Results highlighted the influence of the regularization parameters - introduced to control the balance beetwen the two competing terms, namely the data term and the regularizer - on the description of the small scales. In addition, these observations emphasized the need to objectify the choice of these parameters values. A peculiar attention will be paid on the relation beetwen this parameters and the main physical scales involved in the particule images.

4.1.5 FLUID project database

OF1 approach was evaluated on synthetic sequences of particle and scalar images based on a DNS of 2D turbulent flow (see §2.5 cases C1a and C1b). Since the flow was 2D the optical flow constraint equation (OFCE) was considered for the data term (see eq. 3.1). In order to preserve the divergence and the vorticity of the displaced motion field a second order Div-Curl regularization was used (see §3.1.4).

Figure 4.12a presents the RMS of the error for the whole sequence of case C1a (particle images). Results show that OF1 approach provided values for the RMS of the error lying between 0.12 and 0.13 pixels. This level of error was low but higher than the levels observed

for OF2 approach and for LaVision correlation approach[1] lying between 0.07 - 0.08 pixels and 0.075 - 0.085 pixels, respectively. The map of vorticity and the vector fields presented in figure 4.14 yield the noisy results provided by OF1 approach. Figure 4.13 also shows the high level of noise generated by OF1 approach compare to OF2 approach and LaVision correlation approach. This behaviour of OF1 approach was due to:

- the scheme involving auxiliary function to simplify the numerical solving of the 2nd order div-curl regularization (see §3.1.4);
- the bilinear interpolation scheme used to warp the image;
- the Gaussian derivative filter used to compute the gradients of the luminance.

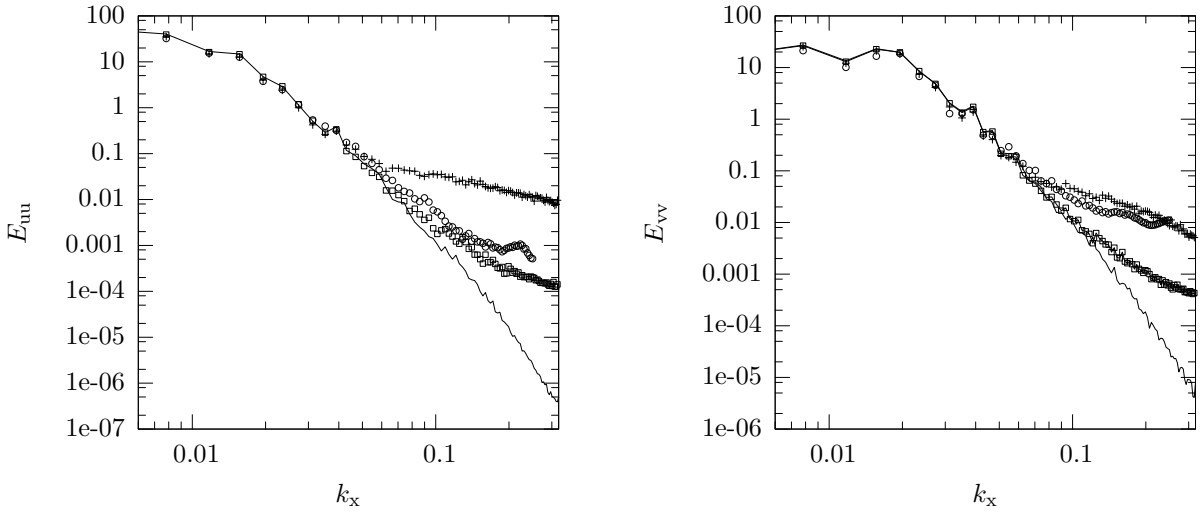

Figure 4.13: Spectra of the velocity extracted from images of particles (case C1a FLUID project database) with: (-), DNS; (+), OF1 approach; (□), OF2 approach; (○) correlation technique.

Figure 4.12b presents the RMS of the error for the whole sequence of case C1b (scalar images). Results exhibit that the RMS of the error was larger for that case compared to the case C1a with particle image. As time evolved, the scalar was dispersed by turbulent and molecular diffusion and the RMS of the error increased sligthly for optical flow approaches. On the contrary the results provided by LaVision with correlation technique (computed by Bernd Wieneke with interrogation windows of 16×16 pixels and 75% overlap) showed decreasing errors as time evolved. The correlation algorithm had problems with gradient images at the rim of the image. Hence, a rim of 20 pixels were taken away because it was too noisy anyway. It is worth noting and not surprinsing that for scalar image optical flow approaches provided better results than correlation technique. It should also be mentioned that during the time sequence the parameter of the regularization term was adjusted in order to minimize the error. The adjustement was link with the drecreasing number of grey levels in the images. In figure 4.15 renormalized scalar images at three differents time steps (beginning, middle and end of the time sequence) indicate the range of grey level involved. As a function of the time, the narrowing of the range of grey level, leading to higher noise, could explain the slight increasing of errors provided by optical flow approaches. However, the present results also show that despite OF1 approach was able to provide smaller errors than the correlation technique, it is observed in figures **??**, 4.16 and 4.17 – presenting respectively the vector field, the vorticity map and the energy spectrum – that the large and the small scales were poorly described. In this case the noise provided by

[1]Results processed by B. Wieneke with 8×8 interrogation window with gaussian weighting function.

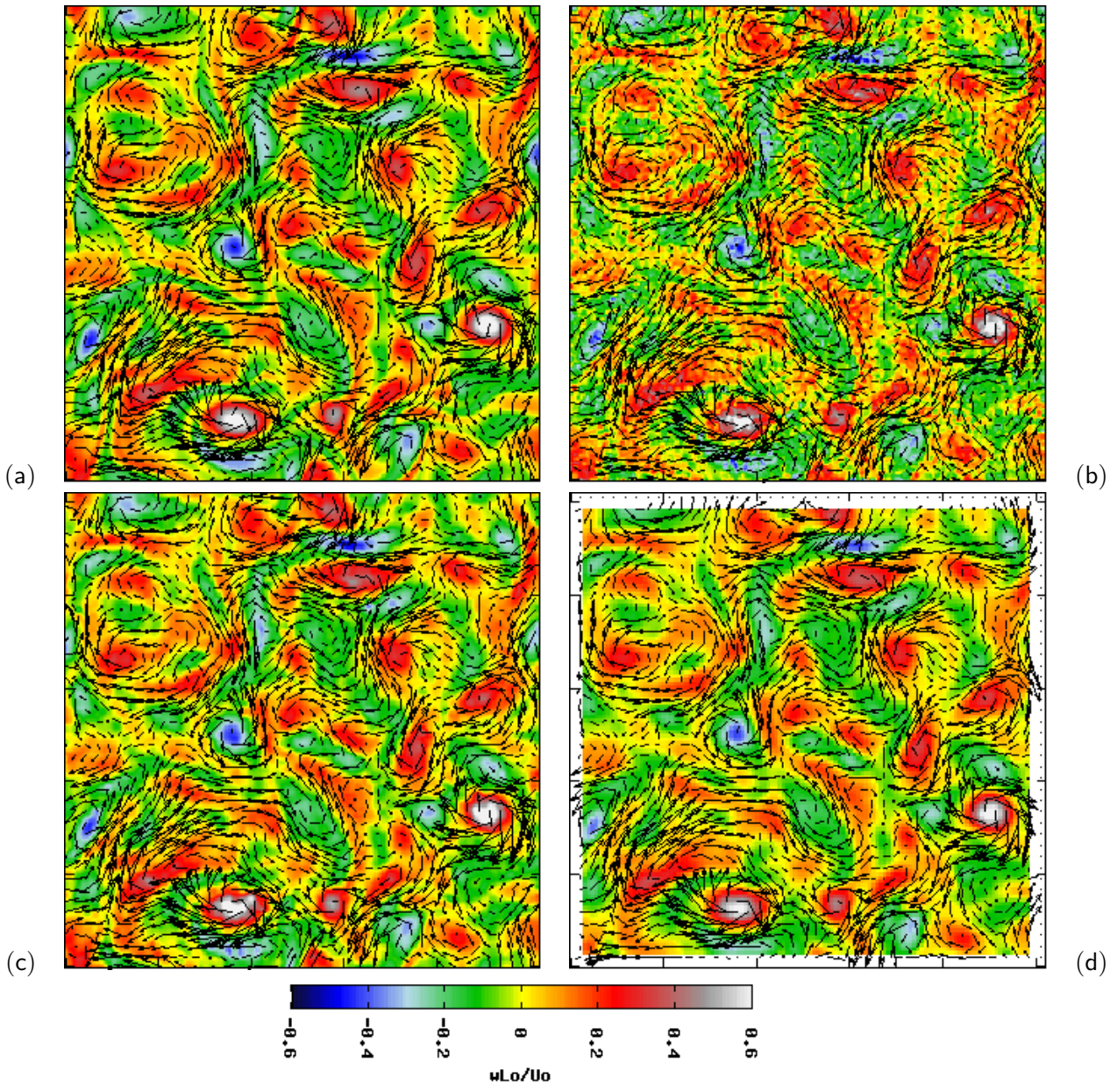

Figure 4.14: Intantaneous vector fields and vorticity maps extracted from images of particles in 2D turbulent flow (case C1a FLUID project database) with: (a), DNS; (a), OF1 approach; (c), OF2 approach; (d), correlation technique.

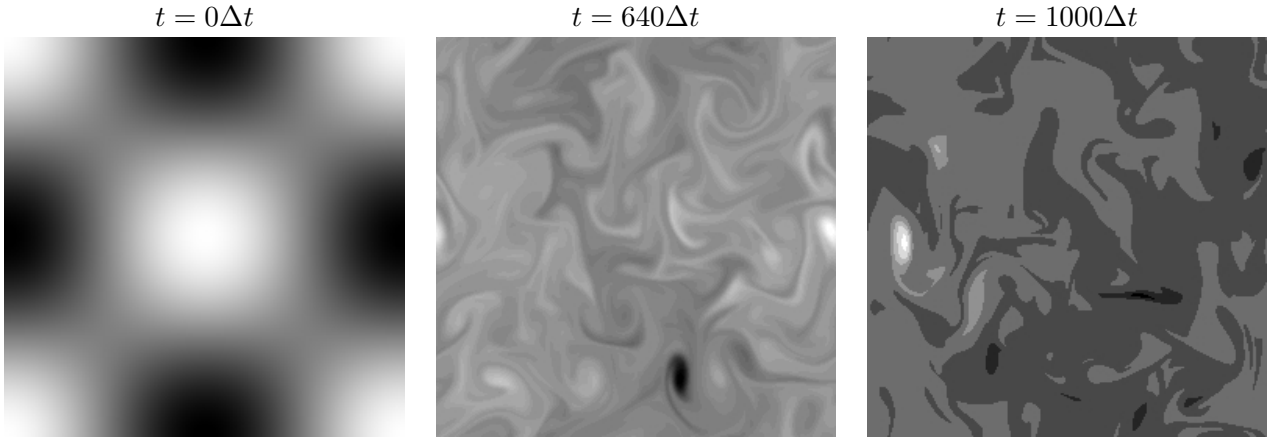

Figure 4.15: Typical image of scalar of case C1b used to process the quantities showed in figures **??**, 4.16 and 4.17.

the numerical schemes (see the three items above), by the decreasing (as time evolved) range of grey level, explained only partly the discrepancies observed beetwen the OF1 approach and the DNS. The other part could be due to the unadequacy of the data term (OFCE model) which did not take into account the molecular diffusion of the scalar. Let us recall that for the case C1b the scalar was adjusted with the Schmidt number $Sc = 0.7$ and the Peclet number $Pe = 2000$ to behave like the temperature. Furthermore, due to the different sources of noise, the robust minimization reduced the importance of the data term for the benefit of the regularization term, thus allowing divergence.

An attempt wase also made to evaluate OF1 approach on real particle images generated for the FLUID project. For that purpose we used the case D1 corresponding to the experiment in the far wake of a circular cylinder at $Re = 3900$ (see §2.6 for details). Unfortunately, OF1 was not able to extract any acceptable displacement fields. This problem was due to the multiresolution technique, designed to estimate multiscale motion, which smoothed out the small particles with large velocities. Indeed, this set of images contained mainly small particles around 2 pixels which had large displacements around 15 pixels. Unsurprisingly, OF2 approach was also not able to extract any acceptable displacement fields. In §3.3 and 4.3, a new approach combining correlation and optical flow was proposed to overcome this obstacle.

4.1.6 Conclusion

In this preliminary evaluation OF1 approach was analysed. This method is an extension of the standard optical-flow based approaches used in Computer Vision where a robust objective function is minimized. The two parts (i.e, the data term and the regularizer) of the novel cost function have been specifically designed to suit image sequences of fluid flows (Corpetti *et al.*, 2002*a*, 2006).

The data term is based on a continuity equation, as a more physically-grounded alternative to the usual brightness constancy assumption in the general case of images of 3D flows. To be compatible with large displacements, it is used in an integrated form. As for the regularization, it is stated that only a second-order regularizer is able to preserve completely the divergence and vorticity structures of the flows. Using the div-curl formalism, a second-order regularizer is introduced to capture the divergence and vorticity of the unknown flow.

The developped approach was tested on synthetic images from the VSJ, on two experimental flows representing a mixing layer and the near wake of a circular cylinder, on the cases of the PIV Challenge 2005 and on some cases of the database dedicated to the FLUID project. In

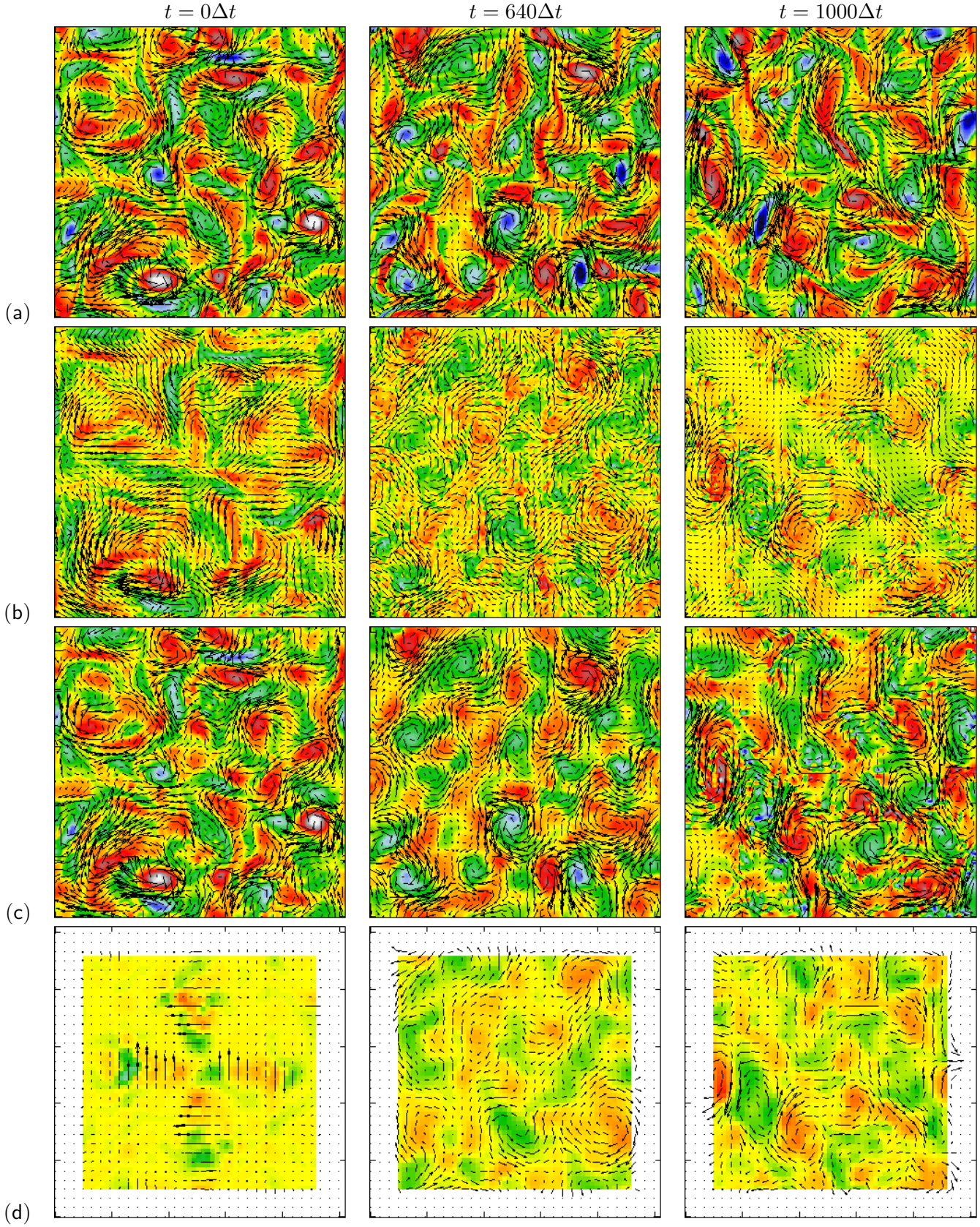

Figure 4.16: Map of vorticity extracted from images of scalar (case C1b FLUID project database) with : (a), DNS; (b), OF1 approach; (c), OF2 approach; (d), correlation technique; at three time steps.

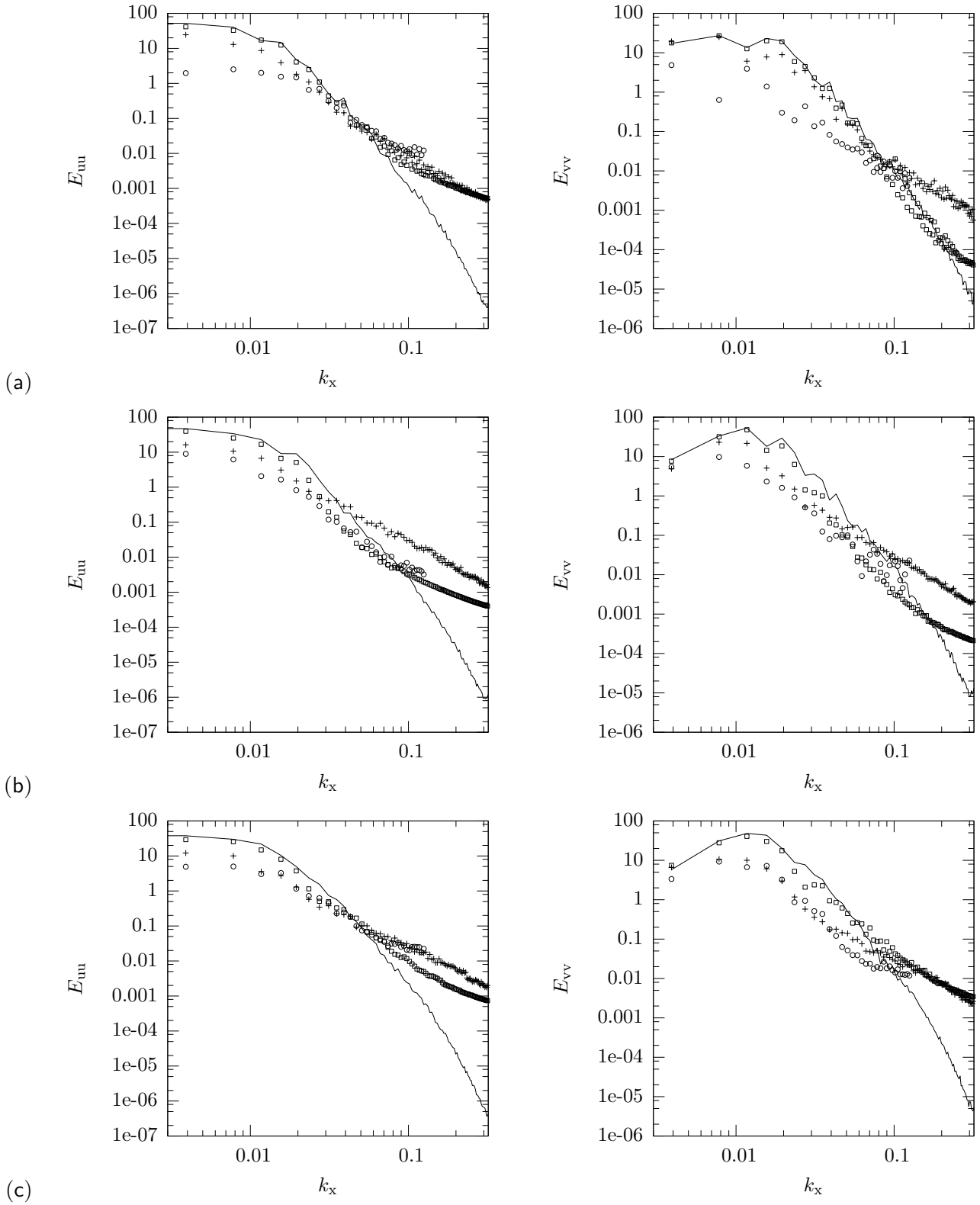

Figure 4.17: Spectra of the velocity extracted from images of scalar (case C1b FLUID project database) with: (-), DNS; (+), OF1 approach; (□), OF2 approach; (◇), correlation technique; at three time steps: (a), $t = 0\Delta t$; (b), $t = 640\Delta t$; (b), $t = 1000\Delta t$.

each case, the results were compared with the motions estimated with correlation techniques and hot-wire anemometry.

It is pointed out that the displacements fields extracted with OF1 and correlation methods have the same order of magnitude. The relevance of the obtained motion fields is then similar. A major difference comes from the number of vectors that optical-flow technique is able to estimate, one vector per pixel being obtained, what opens an ability to describe a larger range of velocity scales than correlation approach. Preliminary results, showed that the dynamic range was enlarged towards smaller scales. However, it was also shown that these methods involved parameters that need to be better known and "calibrated" to improve the results, and also that OF1 provided noise at small scales that could be reduced with improved numerical schemes. The present evaluation also exhibited better velocity estimations for OF1 approach compared to correlation schemes. Despite a poor agreement with the DNS velocity reference, OF1 approach yielded better velocity estimations than correlation schemes, for scalar images. The discrepancies were partly explained by the diffusion of the scalar that was not modelized in the data term. For the following evaluation, this suggested on one hand to develop a data term including this physical phenomena, and on the other hand to provide a new set of data images of a scalar that would not diffuse by molecular process.

4.2 Variational motion estimation for incompressible flows

OF2 approach was evaluated on synthetic sequences of particle and scalar images based on a DNS of 2D turbulent flow (see §2.5 cases C1a and C1b). The method is dedicated to 2D divergence free flows and includes a high-order regularization term that preserves the vorticity (see §3.2).

Quantitative evaluation displayed in figures 4.12a, 4.13 and 4.14 show that OF2 method yielded better results than other competitive methods like OF1 and the correlation technique provided by LaVision. This good agreement with DNS vector fields may be explained by the additional constraint that encouraged solenoidal solutions. However, the use of mimetic finite difference scheme to formulate the estimation problem, the use of spline to warp the images and compute the gradients had also a contribution these nice results. It should be noticed that unfortunately the results obtained with OF2 method for the whole image sequence and displayed in figures 4.12, 4.13 and 4.14 were computed with non optimized regularization parameter equaled to 0.002. Indeed, figure 4.18, show spectrum obtained with different values of the regularization parameter λ, showing that the optimum was around $\lambda = 0.005$.

Quantitative evaluations on scalar image presented in figures 4.12b, 4.17, **??** and 4.16 demonstrate that OF2 method outperformed OF1 approach and the correlation technique proposed by LaVision. Like for OF1, better results could have been provided by OF2 if the molecular diffusion of the scalar had been modelized in the data term, or if no diffusion of the scalar had been included in the DNS.

In the following evaluations we will observe if these convincing results obtained with OF2 approach will still be possible with synthetic and real image sequence of 3D turbulent flows.

An attempt wase also made to evaluate OF2 approach on real particle images generated for the FLUID project. For that purpose we used the case D1 corresponding to the experiment in the far wake of a circular cylinder at $Re = 3900$ (see §2.6 for details). Unfortunately, for the same reasons than for OF1 (see §4.1.5), OF2 was not able to extract any acceptable displacement fields.

4.3 Collaborative correlation-optical flow scheme

In this section we present the results obtained for COROF1 approach (see §3.3.4) with data images of the FLUID project database (see §2.5, §2.6 and §2.7).

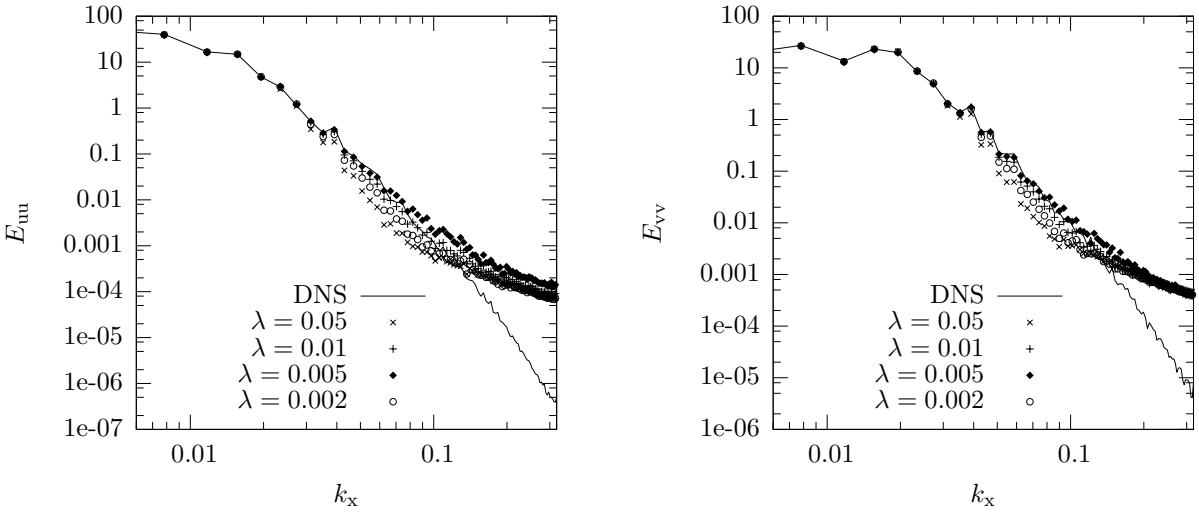

Figure 4.18: Influence of the regularization parameter λ on the spectrum of the vertical velocity component estimated with OF2 method – 2D turbulent flow (case C1a).

4.3.1 Numerical evaluation

This section compares results on DNS-based synthetic image sequence obtained with the following approaches:

- *Correlation:* To estimate correlation-based velocity fields, the commercial software DaVis 7.2 from LaVision was used. A multipass algorithm with a final interrogation window size of 16×16 px^2 and 50% overlapping was applied. Image deformation and round gaussian weigthing function were used. Spurious velocities were identified with median filter and replaced by the median. The vector fields obtained with this correlation technique were used in the collaborative approach.

- *Multiresolution OF2:* This fluid dedicated optical flow approach uses second-order regularization and multiresolution to handle large displacements (see §3.3.2 for details)

- *Dynamic consistent multiresolution (see Deliverable 5.5):* This approach is an extension of the fluid dedicated approach of Corpetti *et al.* (2006) with a spatio-temporal constraint satisfying the Naviers-Stokes equations.

- *Correlation variational COROF1:* This collaborative approach is an adaptation of Corpetti *et al.* (2006) approach to handle large displacements with correlation instead of multiresolution.

- *Dynamic consistent correlation-variational COROF2 (see Deliverable 5.5)*: As described above, this approach uses second-order regularization, correlation to handle large displacements, dynamic consistency satisfying Navier-Stokes equations.

For all approaches the same set of parameters was used, providing an optimal performance: $\alpha = 1000$, $\beta/\alpha = 1$ with $\sigma = 8$ px and $\gamma/\alpha = 0.05$

Synthetic image sequence

To evaluate the performanec of the collaborative approach compare to state of the art optical-flow and correlation approaches, a synthetic particle image sequence was generated based on the direct numerical simulation (DNS) of 2D turbulent flow (Carlier & Wieneke, 2005). The present

flow contains typical difficulties for image based measurements techniques, like high velocity gradients and large dynamic range. The Reynolds number based on the length scale of domain of computation 2π and on the rms of the forcing velocity was equal to 30 000. Figure 4.19 presents the whole flow domain and the region considered for a thorough comparison.

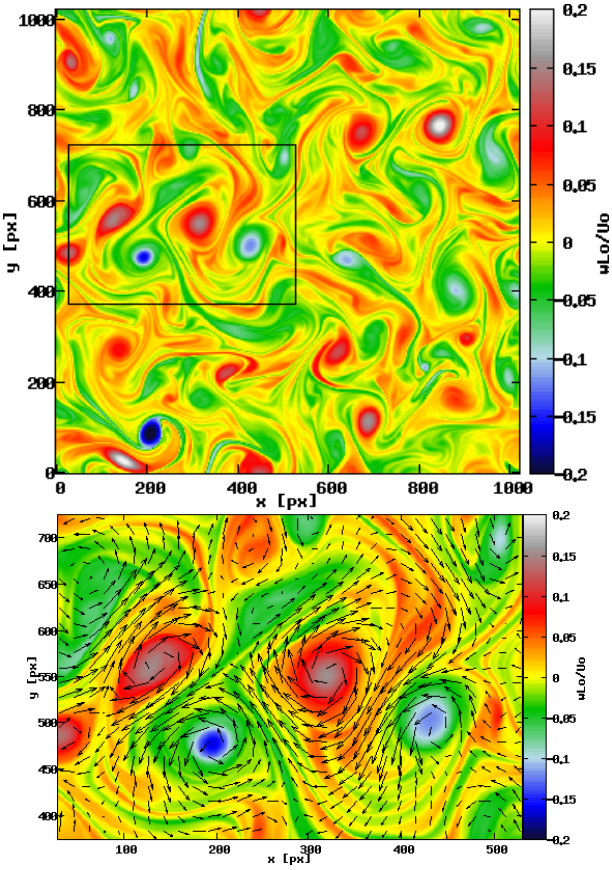

Figure 4.19: 2D turbulence test case - Color map of the normalized vorticity with superposed velocity field.

The image sequence was generated with a home-made particle image generator involving comparable methods than those developed for the EUROPIV Synthetic Image Generator (Lecordier & Westerweel, 2003). A velocity-vorticity formulation of the Navier-Stokes equations was adopted for the DNS. The vorticity equation was solved in Fourier space using desaliased Fourier expansions in two directions with periodic boundary conditions. The time integration was third-order/three steps with a Runge-Kutta scheme. The code is called pseudo-spectral. The coordinates of each particules were calculated in the physical space inside the vorticity equation computation using the Runge-Kutta scheme of the DNS in order to use the intermediate velocity components. However, a bicubic interpolation of the velocity field was applied since the particles were not supposed to be located at the nodes of the grid.

In the present evaluation the image pair considered led to a maximum particle image displacement up to 6 pixels. This particle image displacement was globally optimum to minimize the RMS error provided by the variational technique. This relatively small maximum displacement necessitates a multiresolution pyramid with only two levels. However, the addition of noise in the image pairs enables to put variational techniques, involving multiresolution scheme, on the wrong track.

In order to provide more realistic conditions the signal to noise ratio was increased, simulating a reduction of the power of the virtual laser (Hain & Kähler, 2007). The noise wase quantified with peak signal-to-noise ratio (PSNR) which is the ratio between the maximum possible power

of a signal and the power of corrupting noise that affects the fidelity of its representation. Because many signals have a very wide dynamic range, PSNR is usually expressed in terms of the logarithmic decibel scale. The PSNR is most commonly used as a measure of quality of reconstruction in image compression. The PSNR is defined as:

$$PSNR = 10\log_{10}\left(\frac{d^2}{MSE}\right)$$

where d is the dynamic of the grey level of the signal, here the particles. For an image where the particle are respresented over 8 bits $d = 2^8 - 1 = 255$. MSE is the mean squared error, which for two $m \times n$ images I_o and I_r where one of the images is considered a noisy approximation of the other, is defined as:

$$MSE = \frac{1}{mn}\Sigma_{i=0}^{m-1}\Sigma_{j=0}^{n-1}||I_o(i,j) - I_r(i,j)||^2$$

Typical PSNR values for images of good quality lie between 30 and 40 dB.

Multiresolution limitations

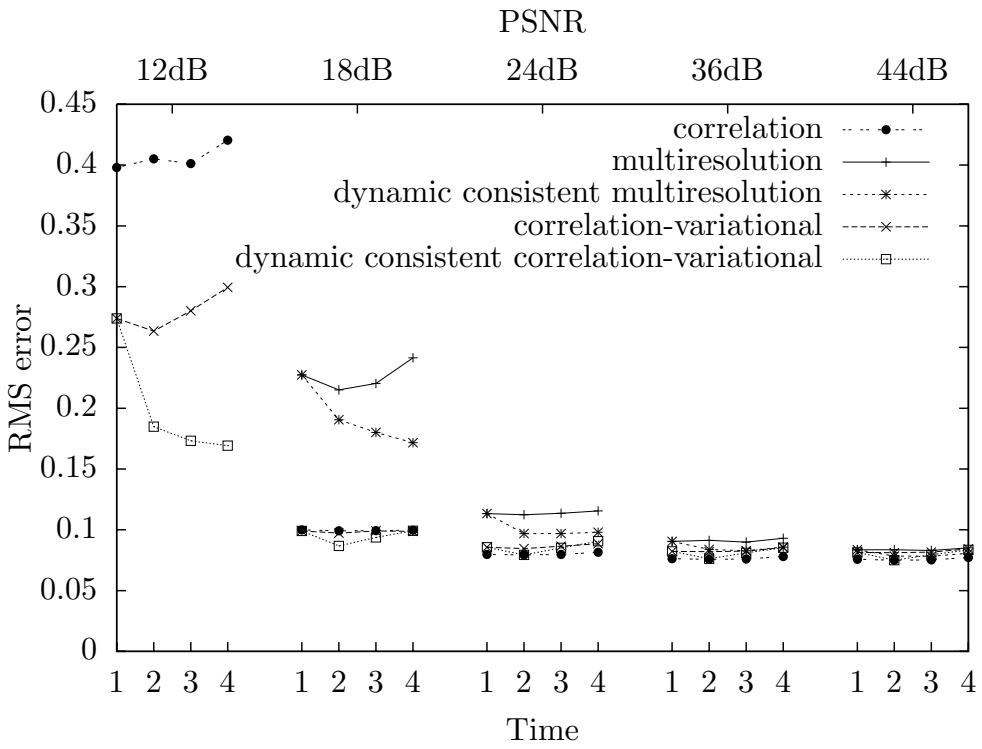

Figure 4.20: RMS of the error of the horizontal velocity component.

In figure 4.20 the RMS error of the approaches is given as a fucntion of the time for five image sequences caracterised by different signal to noise ratio. The same velocity field was used to generate the five image sequences. For all methods the RMS error was increasing whith decreasing values of PSNR (increasing noise). Whatever the value of PSNR, the highest error appeared for the variational approach using the multiresolution scheme (Corpetti *et al.*, 2006). For images of good quality (i.e. PSNR $\geq$ 30 dB), this slight larger error compared to the most competitive correlation approaches, is mainly due to the numerical scheme used to mimic second order regularization (Heitz *et al.*, 2006). For PSNR $<$ 30 dB, image noise influence in the estimated velocities was observed. For images of poor quality (i.e. PSNR = 12 dB) quality, the large error was mainly explained by the inacurrate estimation of the large displacements. Figure

4.21 clearly illustrates this behaviour. It shows the vector field of the exact solution for region of large displacements (for $||\mathbf{u}||/||\mathbf{u}||_{\max} > 30\%$, i.e. for displacements larger than 2 pixels) and the map of color of the deviation of optical-flow from the exact velocity modulus. For regions of large velocities the deviation from the exact solution ranged beetwen 40 % and 100 %. Small particles with large displacements in the images were smoothed out by the down sampling of the multiresolution scheme. In these regions the real motion information was lost. This effect is further promoted by the addition of noise in the images.

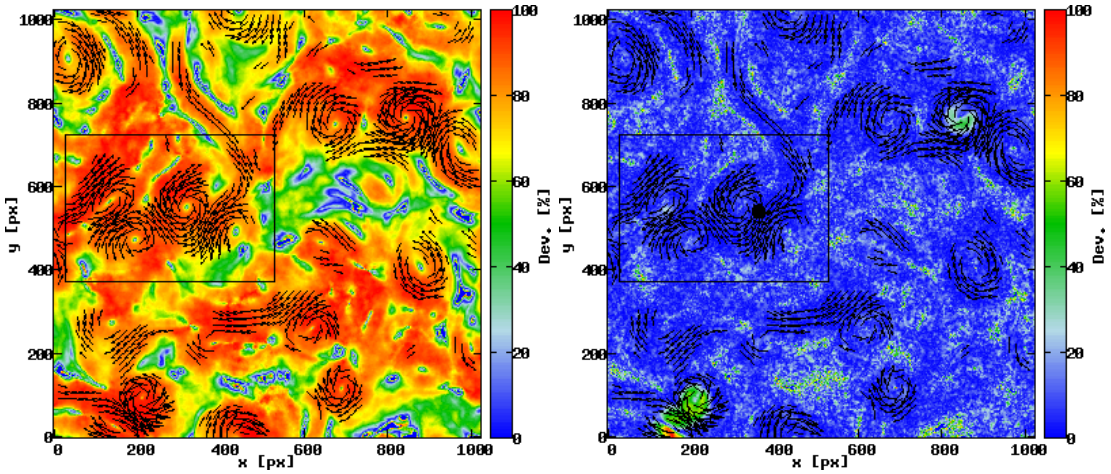

Figure 4.21: Map of color of the deviation of Corpetti *et al.* (2006) from the exact velocity modulus – Vector field of the exact solution for $||\mathbf{u}||/||\mathbf{u}||_{\max} > 30\%$. Top: PSNR = 12 dB; Bottom, PSNR = 24 dB.

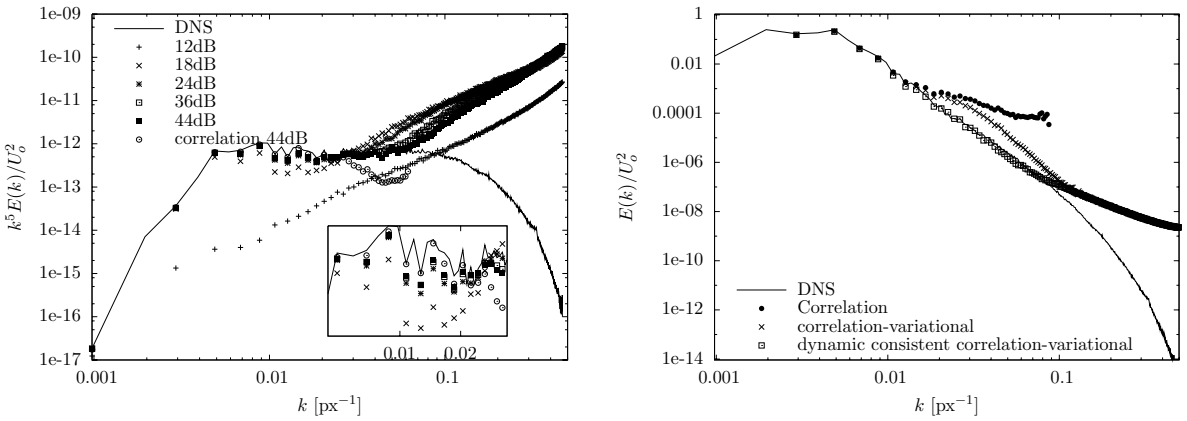

Figure 4.22: Compensated energy spectra: Left, multiresolution approach of Corpetti *et al.* (2006) for different levels of noise in the images; Right, Comparisons between different approaches for PSNR=12dB.

The inaccurate estimation of the large displacements led to a poor extraction of the dynamic especially at large scales. This phenomenon was observed in figure 4.22 by considering the compensated energy spectra to observe the behaviour at large scales. For PSNR = 12 dB, the optical-flow approach completely failed to estimate the dynamic in the flow. For PSNR = 18 dB, the large displacements were more precisely measured. As indicated in figure 4.21, the deviation from the exact solution was smaller. However, figure 4.22 shows for PSNR = 24 dB that, despite the better determination of the large velocities, some discrepancies remained in the description of the largest scales. This behaviour at large scale explained the lack of performance of the scheme proposed by Corpetti *et al.* (2006) compared to the correlation technique considered in

this study, see figure 4.20. As discussed above the accurate optical flow scheme proposed by Yuan *et al.* (2007), using mimetic finite difference to compute second order regularization, would provide the better results, with an enlarged dynamic range.

Collaborative approach

As shown in figure 4.20 the collaborative approach resulted in lower RMS error. The proposed technique allowed the estimation of the large displacements with a deviation from the exact velocity modulus lower than 5% (see Fig. 4.23). The benefit of the collaborative technique was especially observed for image sequences with large noise. In addition this scheme provided a denoising of velocity fields leading to an enlargement of the extracted dynamic range. The improvement that could be gained with the proposed approach is exhibited in figure **??**, giving the distribution of the energy estimated as a function of the spatial scale. The results is quite successful. The collaborative approach provided a robust over noise and dense estimations. It should be noticed that, in the present case due to the use of non accurate second order regularizer, the contribution of the data term of the variational approach was poor. As indicated by the parameters we manualy set for best performance, the proposed correlation-variational global scheme, behaved mainly as a regularizer of the correlation vector fields. Better results should be obtained with more accurate global variational techniques.

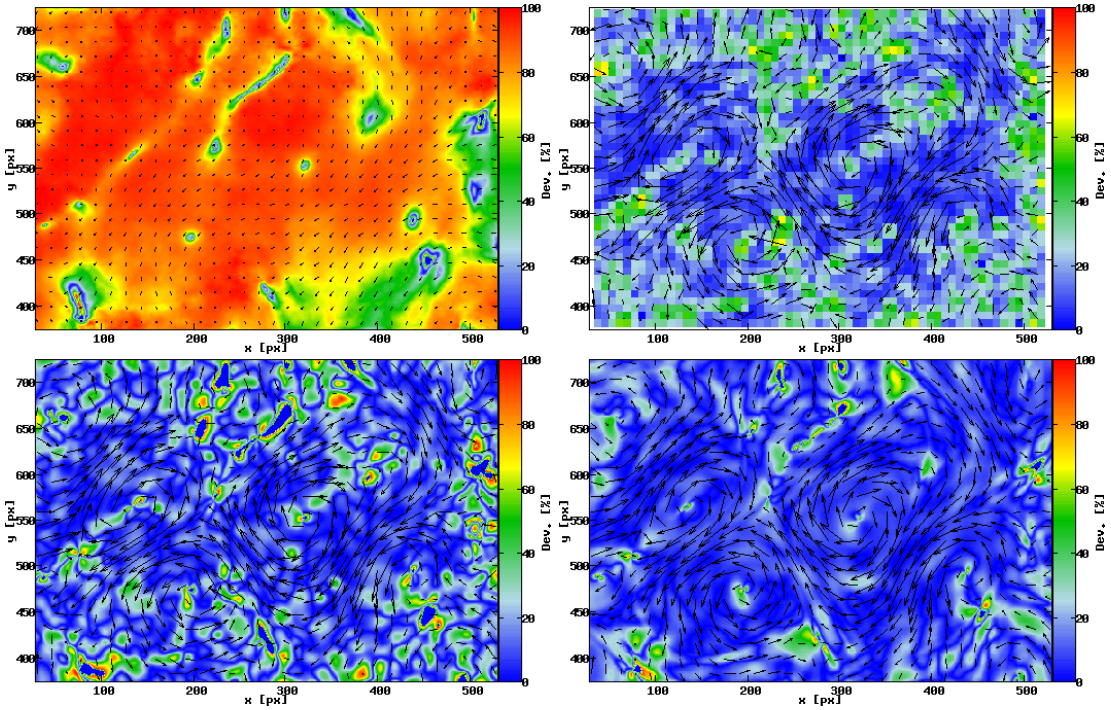

Figure 4.23: Deviation of different approaches from the exact velocity modulus and corresponding vector field – From left to right and top to bottom: multiresolution, correlation, correlation-variational, dynamic consistent correlation-variational. PSNR = 12 dB.

4.3.2 Experimental evaluation

The collaborative approach was also applied to a PIV image sequence recorded in one of the wind tunnels of the Rennes regional Center of the Cemagref. The sequence shows the near wake flow of a circular cylinder at Reynolds number $Re = 3900$ (see §2.6 for details).

The correlation-based velocity fields were calculated with the commercial software DaVis 6.2 from LaVision. A multipass algorithm with a final interrogation window size of 16×16 px^2 and

50% overlapping was applied. Image deformation and round gaussian weigthing function were used. Spurious velocities were identified with median filter and replaced by the median.

Figure 4.24 shows the estimated velocity fields using optical flow technique (Corpetti *et al.*, 2006) and the proposed correlation-variational approach. Optical flow method under-estimated the external high velocity which was approximately two times smaller than the ground truth. This large error was reduced significantly by using the porposed collaborative approach. In figure 4.25, the vorticity color map of correlation-based and collaborative approaches are shown. Less noisy vorticity map were provided by the collaborative scheme, associated with a finer description of the flow. This evaluation with experimental data indicated that the proposed collaborative approach yielded reliable results where classical optical flow techniques failed, with enlargement towards small scales of the spatial description compared to correlation-based technique.

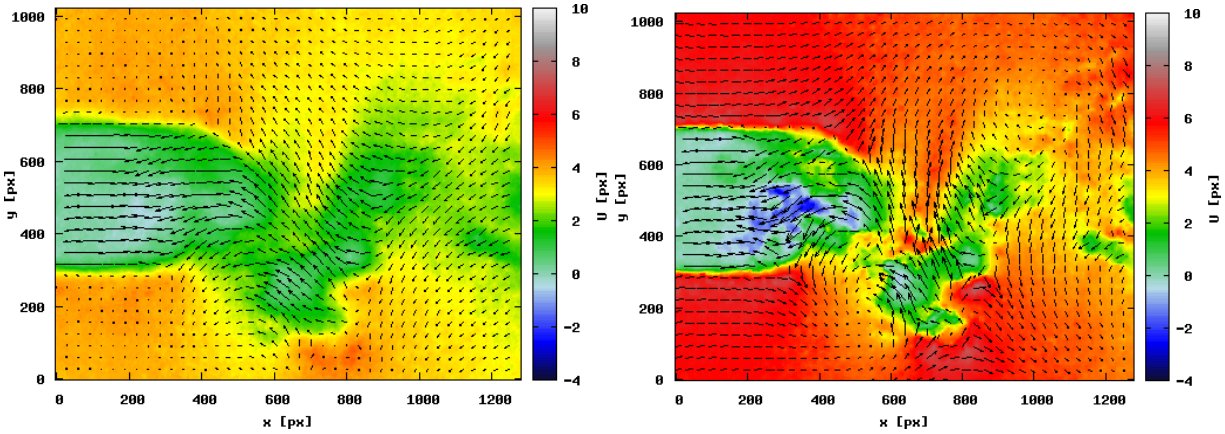

Figure 4.24: Instantaneous vector field with horizontal velocity color map, in near the wake of a circular cylinder at $Re = 3900$. Left, optical-flow approach(Corpetti *et al.*, 2006); Right, COROF1 collaborative approach.

This behaviour was also observed in figure 4.26, where the correlation-variational approach provided a finer description of the flow structure compared to results provided by the correlation approach.

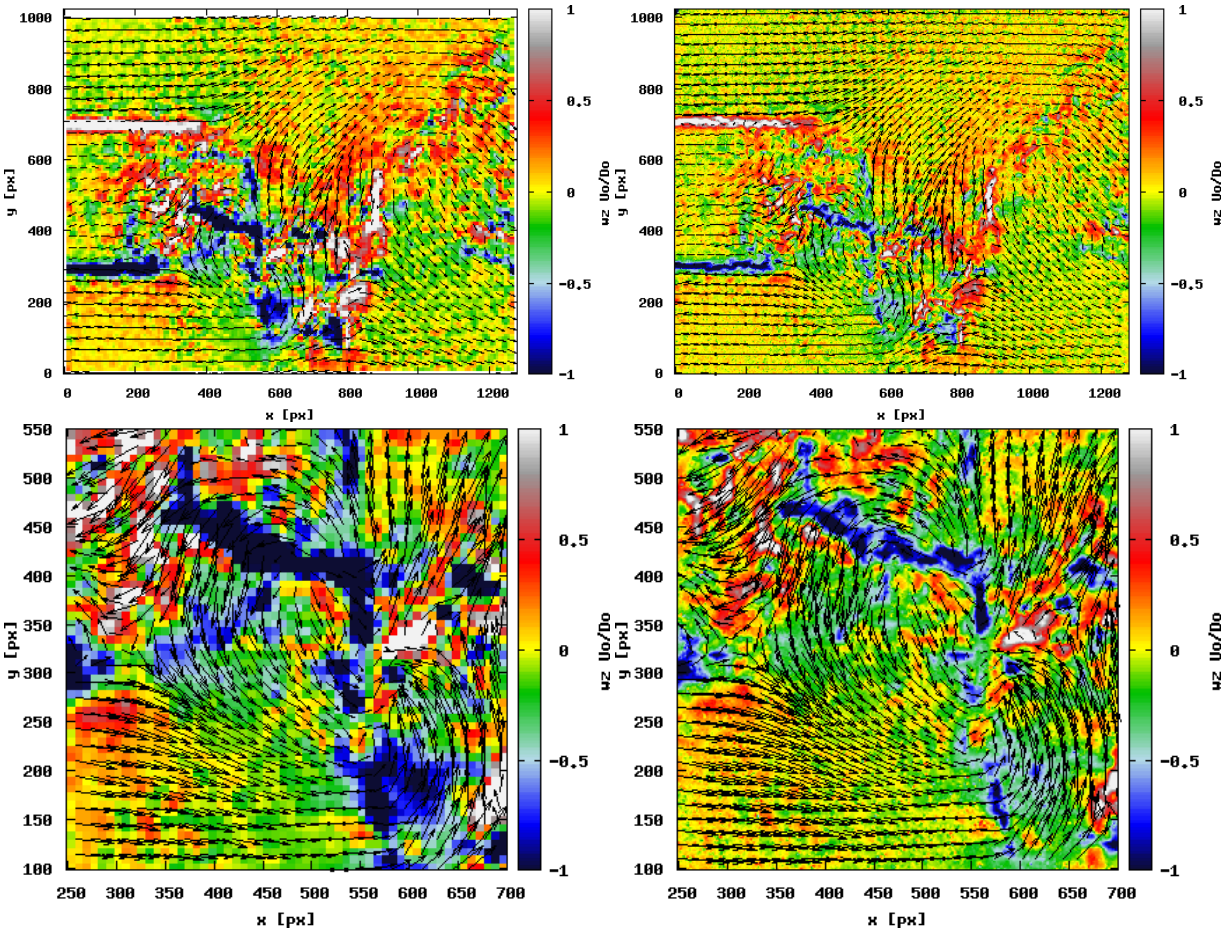

Figure 4.25: Instantaneous vector field with vorticity color map, in near the wake of a circular cylinder at $Re = 3900$. Left, correlation approach; Right, COROF1 collaborative approach.

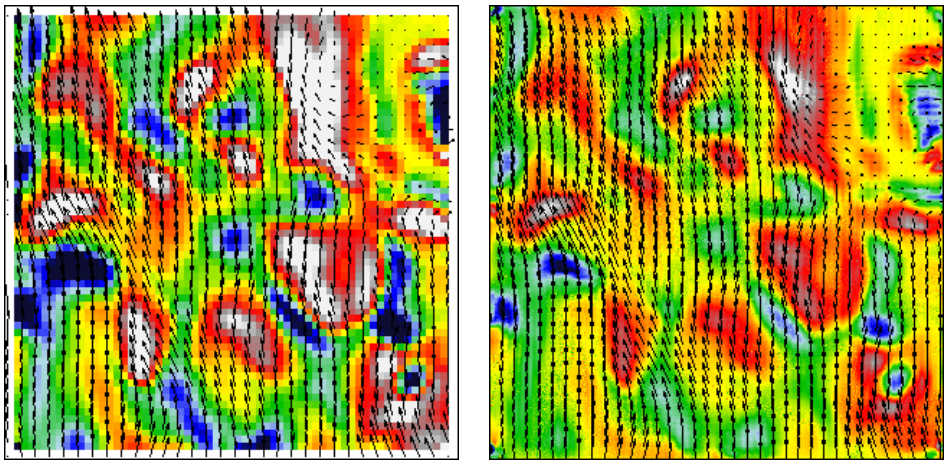

Figure 4.26: Instantaneous vector field with vorticity color map in a slightly turbulent air flow (see §2.7 for details). Left, correlation approach; Right, COROF1 collaborative approach.

Appendix A

A.1 Div-Curl vs first-order regularization

By using the *Euler-Lagrange* condition of minimality, the equivalence between a standard first-order smoothness regularization, and a div-curl regularization with same weights for div and curl penalties can be readily demonstrated. Recall that Euler-Lagrange equation constitutes a necessary conditions for the minimization with respect to function $g(x, y)$ of a functional

$$\int_{\Omega} \mathcal{F}(g, g_x, g_y, x, y) d\boldsymbol{s}.$$

It reads:

$$\frac{\partial \mathcal{F}}{\partial g} - \frac{\partial}{\partial x}\frac{\partial \mathcal{F}}{\partial g_x} - \frac{\partial}{\partial y}\frac{\partial \mathcal{F}}{\partial g_y} = 0$$

Assuming a first-order regularization term

$$\mathcal{H}_{reg}(\boldsymbol{d}) = \alpha \int_{\Omega} (|\boldsymbol{\nabla} u(\boldsymbol{s})|^2 + |\boldsymbol{\nabla} v(\boldsymbol{s})|^2) d\boldsymbol{s},$$

this condition amounts to the following coupled PDEs:

$$\left\{ \begin{array}{rcl} -2\alpha u_{xx} - 2\alpha u_{yy} & = & 0 \\ -2\alpha v_{xx} - 2\alpha v_{yy} & = & 0. \end{array} \right. \tag{A.1}$$

Now, considering a div-curl regularization

$$\mathcal{H}_{reg}(\boldsymbol{d}) = \int_{\Omega} \Big(\alpha \ \mathrm{div}^2 \boldsymbol{d}(\boldsymbol{s}) + \beta \ \mathrm{curl}^2 \boldsymbol{d}(\boldsymbol{s}) \Big) d\boldsymbol{s}, \tag{A.2}$$

the Euler-Lagrange equations reads:

$$\left\{ \begin{array}{rcl} -2\alpha u_{xx} - 2\beta u_{yy} - 2(\alpha - \beta) v_{xy} & = & 0 \\ -2\beta v_{xx} - 2\alpha v_{yy} - 2(\alpha - \beta) u_{xy} & = & 0. \end{array} \right. \tag{A.3}$$

When $\alpha = \beta$, these equations are the same as (A.1)

A.2 Robust penalization

The main objective of robust estimators is to impose a different penalization for coherent and incoherent data: when the error to minimize is small (*e.g.* data are in accordance with underlying assumptions), the robust function tends to the L_2 quadratic norm; when this error is high (*e.g.* presence of outliers), it tends to attenuate the contribution of the error term (and then to be softer than the quadratic function). Figure A.1 presents a possible shape of such function (the Leclerc penalty function: $f_1(x) = 1 - \exp(-\tau_1 x^2)$).

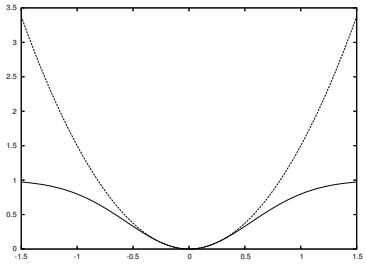

Figure A.1: Comparison of the shape of the Leclerc robust penalisation (bottom) (with $\tau_1 = 1$) *vs* the quadratic one (top)

The choice of robust penalty functions needs to define the parameter τ_1 and generally makes the problem non-quadratic. The specific minimization problem we face is classically turned into an augmented half-quadratic minimization problem Holland & Welsch (1977). Indeed, with all robust penalty functions f such that $f(\sqrt{.})$ is concave (as the Leclerc one), we have the property that:

$$f(x) = \min_{z \in (m,M]} zx^2 + \psi(z), \tag{A.4}$$

where $M = \lim_{0^+} \frac{f'(x)}{2x}$, $m = \lim_{+\infty} \frac{f'(x)}{2x}$, and ψ, for which an expression can be found in Black & Rangarajan (1996); Geman & Reynolds (1992), is such that the minimizer on the right-hand-side is given by $z = \frac{f'(x)}{2x}$.

Using (A.4), each minimization problem of the generic form $\min_x \sum_k f(g_k(x))$ can be replaced by the auxiliary problem $\min_{x,\{z_k\}} \sum_k z_k g_k^2(x) + \psi(z_k)$, which can be solved by iteratively re-weighted least squares (IRLS) Holland & Welsch (1977): for fixed auxiliary (weight) variables $z_k \in (m, M]$, one faces a least-squares problem; for fixed x, the optimal value for each weight is known in closed form as $\frac{f'(g_k(x))}{2g_k(x)}$. This process is done until convergence.

Bibliography

Amini, A. 1994 A scalar function formulation for optical flow. In *Proc. Europ. Conf. Computer Vision*, pp. 125–131. 21

Bannehr, L., Rohn, R. & Warnecke, G. 1996 A functionnal analytic method to derive displacement vector fields from satellite image sequences. *Int. Journ. of Remote Sensing* **17** (2), 383–392. 20

Barron, J., Fleet, D. & Beauchemin, S. 1994 Performance of optical flow techniques. *Int. J. Computer Vision* **12** (1), 43–77. 19

Béréziat, D., Herlin, I. & Younes, L. 2000 A generalized optical flow constraint and its physical interpretation. In *Proc. Conf. Comp. Vision Pattern Rec.*, , vol. 2, pp. 487–492. Hilton Head Island, South Carolina, USA. 21

Bergen, J., Anadan, P., Anna, K. & Hingorani, R. 1992 Hierarchical model-based motion estimation. In *Proc. Europ. conf. Computer Vision* (ed. G. Sandini), pp. 237–252. Springer-Verlag. 28

Bigün, J. & Granlund, G. 1988 Optical flow based on the inertia matrix in the frequency domain. In *Proc. SSAB Symposium on Picture Processing*. Lund, Sweeden. 27

Black, M. 1994 Recursive non-linear estimation of discontinuous flow fields. In *Proc. Europ. Conf. Computer Vision*, pp. 138–145. Stockholm, Sweden. 20

Black, M. & Anandan, P. 1996 The robust estimation of multiple motions: Parametric and piecewise-smooth flow fields. *Computer Vision and Image Understanding* **63** (1), 75–104. 27

Black, M. & Rangarajan, A. 1996 On the unification of line processes, outlier rejection, and robust statistics with applications in early vision. *Int. J. Computer Vision* **19** (1), 75–104. 56

Bloor, M. & Gerrard, J. 1966 Measurements on turbulent vortices in a cylinder wake. *Proc. R. Soc. Lond.* **294**, 319–342. 38

Carlier, J. & Wieneke, B. 2005 Report 1 on production and diffusion of fluid mechanics images and data, Fluid project deliverable 1.2. European Project 'Fluid image analisys and description' (FLUID) – http://www.fluid.irisa.fr/. 47

Cohen, I. & Herlin, I. 1999 Non uniform multiresolution method for optical flow and phase portrait models: Environmental applications. *Int. J. Computer Vision* **33** (1), 29–49. 20, 21

Corpetti, T., Heitz, D., Arroyo, G., Mémin, E. & Santa-Cruz, A. 2006 Fluid experimental flow estimation based on an Optical-flow scheme. *Exp. in Fluids* **40**, 80–97. 1, 9, 19, 27, 43, 47, 49, 50, 52

Corpetti, T., Mémin, E. & Pérez, P. 2002*a* Dense estimation of fluid flows. *IEEE Trans on Pattern Analysis and Machine Intelligence* **24** (3), 365–380. 9, 27, 43

Corpetti, T., Mémin, E. & Pérez, P. 2002*b* Dense estimation of fluid flows. *IEEE Trans on Pattern Analysis and Machine Intelligence* **24** (3), 365–380. 21, 23, 25

Fitzpatrick, J. 1988 The existence of geometrical density-image transformations corresponding to object motion. *Comput. Vision, Graphics, Image Proc.* **44** (2), 155–174. 21

Geman, D. & Reynolds, G. 1992 Constrained restoration and the recovery of discontinuities. *IEEE Trans. Pattern Anal. Machine Intell.* **14** (3), 367–383. 56

Gupta, S. & Prince, J. 1996 Stochastic models for div-curl optical flow methods. *Signal Proc. Letters* **3** (2), 32–34. 23

Hain, R. & Kähler, C. 2007 Fundamentals of multiframe particle image velocimetry (PIV). *Exp Fluids* **42**, 575–587. 48

Héas, P., Mémin, E., Papadakis, N. & Szantai, A. 2007 Layered estimation of atmospheric mesoscale dynamics from satellite imagery. *to appear in IEEE trans. on Geoscience and Remote sensing* . 1, 9, 26

Heitz, D. 1999 Etude expérimentale du sillage d'un barreau cylindrique se développant dans une couche de mélange plane turbulente. PhD thesis, Université de Poitiers. 11, 30, 32, 33

Heitz, D., Héas, P., Mémin, E. & Carlier, J. 2007 Dynamic consistent correlation-variational approach for robust optical flow estimation. *submitted to Exp. in Fluids* . 1, 9, 26

Heitz, D., Navaza, V. & Carlier, J. 2006 Intermediate report on the evaluation of the tasks of the workpackage 2, Fluid project deliverable 5.1. European Project 'Fluid image analisys and description' (FLUID) – http://www.fluid.irisa.fr/. 9, 49

Holland, P. & Welsch, R. 1977 Robust regression using iteratively reweighted least-squares. *Commun. Statis.-Theor. Meth.* **A6** (9), 813–827. 56

Horn, B. & Schunck, B. 1981*a* Determining optical flow. *Artificial Intelligence* **17**, 185–203. 19

Horn, B. & Schunck, B. 1981*b* Determining optical flow. *Artificial Intelligence* **17**, 185–203. 27

Huber, P. 1981 *Robust Statistics*. John Wiley & Sons. 20

Kornprobst, P., Deriche, R. & Aubert, G. 1999 Image sequence analysis via partial differential equations. *Journal of Mathematical Imaging and Vision* **11** (1), 5–26. 20

Larsen, R., Conradsen, K. & Ersboll, B. 1998 Estimation of dense image flow fields in fluids. *IEEE trans. on Geoscience and Remote sensing* **36** (1), 256–264. 21

Lecordier, B. & Westerweel, J. 2003 The EUROPIV Synthetic Image Generator (SIG). In *Particle image velocimetry: recent improvements* (ed. M. Stanislas, J. Westerweel & J. Kompenhans), pp. 145–162. EUROPIV 2 workshop, Springer. 48

Lucas, B. & Kanade, T. 1981 An iterative image registration technique with application to stereo vision. In *Proc. Seventh International Joint Conference on Artificial Intelligence*, pp. 674–679. Vancouver, Canada. 27

Mémin, E. & Pérez, P. 1998*a* Dense estimation and object-based segmentation of the optical flow with robust techniques. *IEEE Trans. Image Processing* **7** (5), 703–719. 20, 29, 30

Mémin, E. & Pérez, P. 1998*b* A multigrid approach for hierarchical motion estimation. In *Proc. Int. Conf. Computer Vision*, pp. 933–938. Bombay, India. 24

Mémin, E. & Pérez, P. 1999 Fluid motion recovery by coupling dense and parametric motion fields. In *Proc. Int. Conf. Computer Vision*, , vol. 3, pp. 732–736. Corfou, Greece. 21

Mémin, E. & Pérez., P. 2002 Hierarchical estimation and segmentation of dense motion fields. *Int. J. Computer Vision* **46** (2), 129–155. 20

Nomura, A., Miike, H. & Koga, K. 1991 Field theory approach for determining optical flow. *Pattern Recognition Letters* **12** (3), 183–190. 22

Okamoto, K., Nishio, S., Saga, T. & Kobayashi, T. 2000 Standard images for PIV. *MST 11* pp. 685–691. 12

Quenot, G., Pakleza, J. & Kowalewski, T. 1998 Particle image velocimetry with optical flow. *Exp. in Fluids* **25** (3), 177–189. 19

Quénot, G. 1999 Performance evaluation of an optical flow technique applied to PIV using the VSJ standard images. In *3rd International workshop on PIV*, pp. 579–584. 12, 29, 30

Ruhnau, P., Kohlberger, T., Schnörr, C. & Nobach, H. 2005 Variational optical flow estimation for particle image velocimetry. *Exp. in Fluids* **38**, 21–32. 12, 21, 29, 30

Schunk, B. 1984 The motion constraint equation for optical flow. In *Proc. Int. Conf. Pattern Recognition*, pp. 20–22. Montreal. 21

Song, S. & Leahy, R. 1991 Computation of 3D velocity fields from 3D cine and CT images of human heart. *IEEE trans. on medical imaging* **10** (3), 295–306. 21

Suter, D. 1994*a* Motion estimation and vector splines. In *Proc. Conf. Comp. Vision Pattern Rec.*, pp. 939–942. Seattle, USA. 22, 23

Suter, D. 1994*b* Motion estimation and vector splines. In *Proc. Conf. Comp. Vision Pattern Rec.*, pp. 939–942. Seattle, USA. 27

Wallace, J. & Foss, J. 1995 The measurement of vorticity in turbulent flows. *Annu. Rev. Fluid Mech.* **27**, 469–514. 21

Wildes, R., Amabile, M., Lanzillotto, A. & Leu, T. 1997 Physically based fluid flow recovery from image sequences. In *Proc. Conf. Comp. Vision Pattern Rec.*, pp. 969–975. 21

Yuan, J., Ruhnau, P., Mémin., E. & Schnörr, C. 2005 Discrete orthogonal decomposition and variational fluid flow estimation. In *Scale-Space 2005, LNCS*, , vol. 3459, pp. 267–278. Springer. 9, 25

Yuan, J., Schnörr, C. & Mémin, E. 2007 Discrete orthogonal decomposition and variational fluid flow estimation. *J. Math Imaging Vis.* **28**, 67–80. 1, 9, 51

Zhou, L., Kambhamettu, C. & Goldgof, D. 2000 Fluid structure and motion analysis from multi-spectrum 2D cloud images sequences. In *Proc. Conf. Comp. Vision Pattern Rec.*, , vol. 2, pp. 744–751. Hilton Head Island, South Carolina, USA. 21